

AD-A265 263



2

AD

TECHNICAL REPORT ARCCB-TR-93010

**PERFORATED BRAKE EFFICIENCY MEASUREMENTS
USING A 20-MM CANNON**

G.C. CAROFANO

DTIC
ELECTE
JUN 03 1993
S B D

MARCH 1993



**US ARMY ARMAMENT RESEARCH,
DEVELOPMENT AND ENGINEERING CENTER
CLOSE COMBAT ARMAMENTS CENTER
BENÉT LABORATORIES
WATERVLIET, N.Y. 12189-4050**



APPROVED FOR PUBLIC RELEASE; DISTRIBUTION UNLIMITED

93 6 02 07 8

93-12473



DISCLAIMER

The findings in this report are not to be construed as an official Department of the Army position unless so designated by other authorized documents.

The use of trade name(s) and/or manufacturer(s) does not constitute an official indorsement or approval.

DESTRUCTION NOTICE

For classified documents, follow the procedures in DoD 5200.22-M, Industrial Security Manual, Section II-19 or DoD 5200.1-R, Information Security Program Regulation, Chapter IX.

For unclassified, limited documents, destroy by any method that will prevent disclosure of contents or reconstruction of the document.

For unclassified, unlimited documents, destroy when the report is no longer needed. Do not return it to the originator.

REPORT DOCUMENTATION PAGEForm Approved
OMB No. 0704-0188

Public reporting burden for this collection of information is estimated to average 1 hour per response, including the time for reviewing instructions, searching existing data sources, gathering and maintaining the data needed, and completing and reviewing the collection of information. Send comments regarding this burden estimate or any other aspect of this collection of information, including suggestions for reducing this burden, to Washington Headquarters Services, Directorate for Information Operations and Reports, 1215 Jefferson Davis Highway, Suite 1204, Arlington, VA 22202-4302, and to the Office of Management and Budget, Paperwork Reduction Project (0704-0188), Washington, DC 20503.

1. AGENCY USE ONLY (Leave blank)		2. REPORT DATE March 1993	3. REPORT TYPE AND DATES COVERED Final	
4. TITLE AND SUBTITLE PERFORATED BRAKE EFFICIENCY MEASUREMENTS USING A 20-MM CANNON			5. FUNDING NUMBERS AMCMS: 6126.24.H180.000	
6. AUTHOR(S) G.C. Carofano				
7. PERFORMING ORGANIZATION NAME(S) AND ADDRESS(ES) U.S. Army ARDEC Benet Laboratories, SMCAR-CCB-TL Watervliet, NY 12189-4050			8. PERFORMING ORGANIZATION REPORT NUMBER ARCCB-TR-93010	
9. SPONSORING / MONITORING AGENCY NAME(S) AND ADDRESS(ES) U.S. Army ARDEC Close Combat Armaments Center Picatinny Arsenal, NJ 07806-5000			10. SPONSORING / MONITORING AGENCY REPORT NUMBER	
11. SUPPLEMENTARY NOTES				
12a. DISTRIBUTION / AVAILABILITY STATEMENT Approved for public release; distribution unlimited			12b. DISTRIBUTION CODE	
13. ABSTRACT (Maximum 200 words) Over the past few years, several field experiments have been performed using 105-mm and 120-mm cannons having perforated muzzle brakes. Significant differences in impulse reduction and gasdynamic efficiency have been reported in tests using the same 105-mm cannon-brake system but different measurement techniques. In the 120-mm experiments, efficiencies considerably above those for the 105-mm cannon have been reported, even though the latter has a larger brake. Because the efficiency is a measure of the load produced by the brake, these inconsistencies introduce some uncertainty as to the stresses generated within the brake. In the present study, five brakes, geometrically similar to those used in the field experiments, were tested in the laboratory using a 20-mm cannon. The purpose was to provide a common basis for comparing the performance of the brakes using the standard parameters of gasdynamic efficiency for impulse and the overpressure ratio for the blast field.				
14. SUBJECT TERMS Muzzle Blast, Muzzle Brake, Perforated Muzzle Brake, Brake Efficiency			15. NUMBER OF PAGES 96	
			16. PRICE CODE	
17. SECURITY CLASSIFICATION OF REPORT UNCLASSIFIED	18. SECURITY CLASSIFICATION OF THIS PAGE UNCLASSIFIED	19. SECURITY CLASSIFICATION OF ABSTRACT UNCLASSIFIED	20. LIMITATION OF ABSTRACT UL	

TABLE OF CONTENTS

ACKNOWLEDGEMENTS	vi
INTRODUCTION	1
THE LABORATORY EXPERIMENT	1
THE GASDYNAMIC SCALING PARAMETERS	2
VELOCITY AND IMPULSE DATA	4
THE SHADOWGRAPHS	6
FREE-FIELD OVERPRESSURE DATA	7
CONCLUSIONS	8
REFERENCES	10
APPENDIX A	31
APPENDIX B	39
APPENDIX C	88

Tables

1. Ballistic Data for the Laboratory Experiment	2
2. Summary of Brake Data	4
3. Field Experiment Data	5
C1. Measured Velocity and Impulse Data	88
C2. Averaged Velocity Data	90
C3. Averaged Impulse Data	90

List of Illustrations

1. Sketch of the six extensions used in the experiments	12
2. Comparison of Eq. (6) with the experimental data	13
3. Shadowgraph of the bare muzzle flow field taken with no time delay (round 19531, Appendix B of Reference 21)	14
4. Shadowgraph of the 120-mm standard brake flow field taken with a 75-microsecond time delay (round 19535, Appendix B)	15

5. Shadowgraph of the 120-mm modified brake flow field taken with a 150-microsecond time delay (round 19538, Appendix B)	16
6. Shadowgraph of the 120-mm side vent brake flow field taken with a 300-microsecond time delay (round 19542, Appendix B)	17
7. Shadowgraph of the 105-mm standard brake flow field taken with a 450-microsecond time delay (round 19566, Appendix B of Reference 21)	18
8. Shadowgraph of the 105-mm elliptic brake flow field taken with a 450-microsecond time delay (round 19570, Appendix B)	19
9. Shadowgraph of the bare muzzle flow field taken with a 750-microsecond time delay (round 19556, Appendix B of Reference 21)	20
10. Shadowgraph of the 120-mm standard brake flow field taken with a 750-microsecond time delay (round 19559, Appendix B)	21
11. Shadowgraph of the 120-mm modified brake flow field taken with a 750-microsecond time delay (round 19562, Appendix B)	22
12. Shadowgraph of the 120-mm side vent brake flow field taken with a 750-microsecond time delay (round 19565, Appendix B)	23
13. Shadowgraph of the 105-mm standard brake flow field taken with a 750-microsecond time delay (round 19569, Appendix B of Reference 21)	24
14. Shadowgraph of the 105-mm elliptic brake flow field taken with a 750-microsecond time delay (round 19572, Appendix B)	25
15. Summary of experimental overpressure data for the bare muzzle case and the 120-mm model brakes	26
16. Summary of experimental overpressure data for the bare muzzle case and the 105-mm model brakes	27
17. Comparison of experimental overpressure data, measured in decibels, for all of the model brakes	28
18. Comparison of experimental overpressure data for the 105-mm model and full-scale experiments	29
19. Comparison of experimental overpressure data for the 120-mm model and full-scale experiments	30
A1. Scaled drawing of the bare muzzle extension	32
A2. Scaled drawing of the 120-mm standard brake	33
A3. Scaled drawing of the 120-mm modified brake	34
A4. Scaled drawing of the 120-mm side vent brake	35

A5. Scaled drawing of the 105-mm standard brake	36
A6. Scaled drawing of the 105-mm elliptic brake	37
B1a. Pressure histories for round 19534, 120-mm standard brake at 30 calibers. Data used in report figures	40
B1b. Shadowgraph for round 19534, 120-mm standard brake, taken with no time delay	41
B2a. Pressure histories for round 19535, 120-mm standard brake at 30 calibers. Data used in report figures	42
B2b. Shadowgraph for round 19535, 120-mm standard brake, taken with a 75-microsecond time delay	43
B3a. Pressure histories for round 19536, 120-mm standard brake at 30 calibers. Data used in report figures	44
B3b. Shadowgraph for round 19536, 120-mm standard brake, taken with a 300-microsecond time delay	45
B4a. Pressure histories for round 19537, 120-mm modified brake at 30 calibers. Data used in report figures	46
B4b. Shadowgraph for round 19537, 120-mm modified brake, taken with no time delay	47
B5a. Pressure histories for round 19538, 120-mm modified brake at 30 calibers. Data used in report figures	48
B5b. Shadowgraph for round 19538, 120-mm modified brake, taken with a 150-microsecond time delay	49
B6a. Pressure histories for round 19539, 120-mm modified brake at 30 calibers. Data used in report figures	50
B6b. Shadowgraph for round 19539, 120-mm modified brake, taken with a 300-microsecond time delay	51
B7a. Pressure histories for round 19540, 120-mm side vent brake at 30 calibers. Data used in report figures	52
B7b. Shadowgraph for round 19540, 120-mm side vent brake, taken with no time delay	53
B8a. Pressure histories for round 19541, 120-mm side vent brake at 30 calibers. Data used in report figures	54
B8b. Shadowgraph for round 19541, 120-mm side vent brake, taken with a 150 microsecond time delay	55

B9a. Pressure histories for round 19542, 120-mm side vent brake at 30 calibers. Data used in report figures	56
B9b. Shadowgraph for round 19542, 120-mm side vent brake, taken with a 300-microsecond time delay	57
B10a. Pressure histories for round 19546, 105-mm elliptic brake at 30 calibers. Data used in report figures	58
B10b. Shadowgraph for round 19546, 105-mm elliptic brake, taken with no time delay	59
B11a. Pressure histories for round 19547, 105-mm elliptic brake at 30 calibers. Data used in report figures	60
B11b. Shadowgraph for round 19547, 105-mm elliptic brake, taken with a 150-microsecond time delay	61
B12a. Pressure histories for round 19548, 105-mm elliptic brake at 30 calibers. Data used in report figures	62
B12b. Shadowgraph for round 19548, 105-mm elliptic brake, taken with a 300-microsecond time delay	63
B13a. Pressure histories for round 19557, 120-mm standard brake at 30 calibers. Data used in report figures	64
B13b. Shadowgraph for round 19557, 120-mm standard brake, taken with a 450-microsecond time delay	65
B14a. Pressure histories for round 19558, 120-mm standard brake at 30 calibers. Data used in report figures	66
B14b. Shadowgraph for round 19558, 120-mm standard brake, taken with a 600-microsecond time delay	67
B15a. Pressure histories for round 19559, 120-mm standard brake at 30 calibers. Data used in report figures	68
B15b. Shadowgraph for round 19559, 120-mm standard brake, taken with a 750-microsecond time delay	69
B16a. Pressure histories for round 19560, 120-mm modified brake at 30 calibers. Data used in report figures	70
B16b. Shadowgraph for round 19560, 120-mm modified brake, taken with a 450-microsecond time delay	71
B17a. Pressure histories for round 19561, 120-mm modified brake at 30 calibers. Data used in report figures	72

B17b. Shadowgraph for round 19561, 120-mm modified brake, taken with a 600-microsecond time delay	73
B18a. Pressure histories for round 19562, 120-mm modified brake at 30 calibers. Data used in report figures	74
B18b. Shadowgraph for round 19562, 120-mm modified brake, taken with a 750-microsecond time delay	75
B19a. Pressure histories for round 19563, 120-mm side vent brake at 30 calibers. Data used in report figures	76
B19b. Shadowgraph for round 19563, 120-mm side vent brake, taken with a 450-microsecond time delay	77
B20a. Pressure histories for round 19564, 120-mm side vent brake at 30 calibers. Data not used in report figures	78
B20b. Shadowgraph for round 19564, 120-mm side vent brake, taken with a 600-microsecond time delay	79
B21a. Pressure histories for round 19565, 120-mm side vent brake at 30 calibers. Data used in report figures	80
B21b. Shadowgraph for round 19565, 120-mm side vent brake, taken with a 750-microsecond time delay	81
B22a. Pressure histories for round 19570, 105-mm elliptic brake at 30 calibers. Data not used in report figures	82
B22b. Shadowgraph for round 19570, 105-mm elliptic brake, taken with a 450-microsecond time delay	83
B23a. Pressure histories for round 19571, 105-mm elliptic brake at 30 calibers. Data not used in report figures	84
B23b. Shadowgraph for round 19571, 105-mm elliptic brake, taken with a 600-microsecond time delay	85
B24a. Pressure histories for round 19572, 105-mm elliptic brake at 30 calibers. Data not used in report figures	86
B24b. Shadowgraph for round 19572, 105-mm elliptic brake, taken with a 750-microsecond time delay	87

DTIC QUALITY IMPROVEMENT

v

Accession For	
NTIS GRA&I	<input checked="" type="checkbox"/>
DTIC TAB	<input type="checkbox"/>
Unannounced	<input type="checkbox"/>
Justification	
By	
Distribution/	
Availability Codes	
Dist	Avail and/or Special
A-1	

ACKNOWLEDGEMENTS

The author would like to thank Mr. Larry Rusch of Benet Laboratories for making the preparations for the experiments and Mr. Doug Savick of the Ballistic Research Laboratory, Aberdeen Proving Grounds, MD, for conducting the experiments and reducing the data. Funding for the experiments was provided by the Project Manager of Tank Main Armaments Systems (PM-TMAS), Picatinny Arsenal, NJ.

INTRODUCTION

Over the past few years, several field experiments have been performed using 105-mm (refs 1-3) and 120-mm (refs 4,5) cannons having perforated muzzle brakes. Significant differences in weapon impulse and gasdynamic efficiency have been reported in tests using the same 105-mm cannon-brake system but different measurement techniques. In the 120-mm experiments, efficiencies considerably above those for the 105-mm cannon have been reported, even though the latter has a larger brake. Because the efficiency is a measure of the load produced by the brake, these inconsistencies introduce some uncertainty as to the stresses generated within the brake. In the present study, five brakes, geometrically similar to those used in the field experiments, were tested in the laboratory using a 20-mm cannon. The purpose was to provide a common basis for comparing the performance of the brakes using the standard parameters of gasdynamic efficiency for impulse and the overpressure ratio for the blast field.

The gasdynamic efficiency is a dimensionless measure of the capacity of a muzzle brake to reduce weapon impulse. Experimental (refs 6-8) and analytical studies (refs 6,9) of conventional baffle brakes have shown that this parameter depends primarily on the brake geometry, and that it is rather insensitive to weapon caliber and only mildly dependent upon ballistics, primarily through the propellant gas Mach number at projectile exit. As a result, brake efficiency has often been determined using scaled models in the laboratory where accurate measurements of impulse are more easily made (refs 6-8,10,11).

Laboratory (refs 12-16) and numerical (refs 17-19) studies have also been made for perforated muzzle brakes. For these devices, the gasdynamic efficiency is primarily dependent on the vent area ratio, (total vent area to cannon bore area), and mildly dependent on the vent aspect ratio (height to diameter) and angle of inclination of the vent axis with respect to the cannon axis. Insensitivity to weapon caliber and ballistics is also characteristic (ref 19).

A second gasdynamic parameter, the overpressure ratio, is used to measure the modifications of the blast field that result when a brake is added to a cannon. It is defined as the ratio of the peak free-field overpressures at a particular location with and without the brake. Its sensitivity to geometry and ballistics is examined here for perforated brakes.

THE LABORATORY EXPERIMENT

The experiment was performed using the 20-mm cannon facility at the Ballistic Research Laboratory. The cannon is threaded at the muzzle to accept the six extensions shown schematically in Figure 1 (scaled drawings may be found in Appendix A). The first four were scaled to the 120-mm experiments (refs 4,5), while the last two refer to the 105-mm experiments (refs 1-3). The bare muzzle extension was used as a reference for both sets of brakes even though the wall thickness was scaled to the 120-mm cannon. This tube dimension is not expected to have a measurable effect on the blast field.

The '120-mm standard' brake has eight rows of circular vents. Each row has twelve vents uniformly spaced around the tube circumference. The four rows nearest the breech have smaller diameter vents based on stress considerations (refs 19,20). The '120-mm modified' brake is identical to the standard brake except that the vents are raked back ten degrees to provide greater impulse reduction.

The '120-mm side vent' brake has nine rows of vents. Each row has only ten vents--five on each side of the vertical axis of the tube. The purpose of this arrangement is to reduce obscuration by directing the gas to the sides of the weapon. The vents are drilled at angles such that the vent area is more uniformly distributed around the tube interior to provide a symmetrical pressure distribution. Large circumferential pressure gradients can damage finned projectiles (ref 1). All three 120-mm brakes have the same total vent area based on the cross-sectional area perpendicular to the vent axis.

The '105-mm standard' brake has twelve rows of circular vents. Each row has twelve vents placed uniformly around the tube circumference. The '105-mm elliptic' brake is similar except that each row has six elliptical vents. Both brakes have the same total vent area.

All of the extensions have the same length. In practice, vented tubes have to be somewhat longer to produce the desired projectile velocity. However, for the 20-mm cannon, the addition was only a few centimeters and was omitted to facilitate comparison of the blast fields.

The ballistic data for the cannon are listed in Table 1. The projectile base position refers to the length of the cannon without an extension. The conditions at this instant are known from earlier experiments (ref 12).

Table 1. Ballistic Data for the Laboratory Experiment

Projectile base position, cm	143.00
Projectile velocity, m/sec	1045.0
Projectile base pressure, atm	287.0
Propellant mass, kg	0.0389
Projectile mass, kg	0.0980
Bore diameter, cm	2.0
Gun chamber volume, cm ³	41.7
Specific heat ratio	1.25
Molecular weight	22.8
Covolume, cm ³ /kg	982.0

THE GASDYNAMIC SCALING PARAMETERS

The gasdynamic efficiency, β , of a brake is defined as

$$\beta = (I_w - I_{w0}) / (I_{w0} - M \cdot V_p) \quad (1)$$

where I_w and I_{w0} are the weapon impulses with and without a brake, respectively, M is the projectile mass, and V_p is the bare muzzle velocity. To appreciate the significance of β in cannon design, it is helpful to rewrite this expression in terms of the internal ballistics and brake geometry using control volume analysis (refs 1,9).

Summing the pressure forces acting on a control volume drawn coincident with the interior and exterior surfaces of the tube, including the vent surfaces, gives the following expression for the impulse, I , imparted to the cannon:

$$I = A \int_0^{\infty} (P_b - P_o) dt - \sum_{n=1}^N \int_0^{\infty} \int_{S_n} P_n n_x dS_n dt \quad (2)$$

The first term is the integral of the unbalanced pressure forces acting upon the tube interior and exterior surfaces. P_b is the time-dependent breech pressure of the propellant gas, P_o is atmospheric pressure, and A is the bore area. The second term is the sum of the integrals of the pressure forces generated by the N individual vents. P_n is the time- and position-dependent pressure acting upon the vent surface S_n , and n_x is the axial component of the unit vector normal to and pointing away from the vent surface element dS_n . Equation (2) applies to a cannon with or without a brake.

For a control volume drawn coincident with the exterior surface of the tube and extending across the muzzle exit plane, the impulse, I_{wo} , for a cannon having no brake is

$$I_{wo} = MV_p + A \int_0^{\infty} (P_e - P_o + \rho_e v_e^2) dt \quad (3)$$

The first term is the momentum of the projectile as its base passes through the muzzle exit plane. The second term is the integral of the thrust produced by the propellant gas as it is discharged through this plane with pressure P_e , density ρ_e , and velocity v_e . P_o is atmospheric pressure.

Using these results in Eq. (1), the expression for β becomes

$$\beta = \frac{A \int_0^{\infty} (P_{bwo} - P_{bw}) dt + \sum_{n=1}^N \int_0^{\infty} \int_{S_n} P_n n_x dS_n dt}{A \int_0^{\infty} [P_e (1 + \gamma M_e^2 / (1 - \eta \rho_e)) - P_o]_{wo} dt} \quad (4)$$

where the subscripts 'w' and 'wo' indicate which variables apply to the brake and the bare muzzle cases, respectively. The denominator was rewritten in terms of Mach number, M_e , using the expression for soundspeed in an Abel gas, namely, $c_e^2 = \gamma P_e / (\rho_e (1 - \eta \rho_e))$ where γ and η are the specific heat ratio and covolume of the propellant gas, respectively.

The first term in the numerator of Eq. (4) requires some explanation. For the cannons of interest here, a region of supersonic flow develops immediately behind the projectile as it accelerates in the tube. The sonic point at the upstream boundary of this region also moves downstream during the ballistic cycle. When it reaches the brake entrance, an expansion wave starts traveling toward the breech. In the bare muzzle case, this event is delayed until the sonic point reaches the muzzle. Therefore, for cannons of equal length, as in the experiments, the expansion wave arrives at the breech earlier in the brake case, causing the pressure P_{bw} to fall relative to P_{bwo} and the integrand $(P_{bwo} - P_{bw})$ to become positive. Calculations with the impulse code (refs 18,19) show that this term generally contributes about two percent to the numerator. For a baffle brake, this term is zero, because the brake is located downstream of the muzzle in the supersonic exhaust flow and cannot influence the flow in the barrel.

According to Eq. (4), β is a function of the cannon ballistics and the brake geometry. However, the ballistics tend to influence the numerator and denominator in the same way. For example, each integrand is proportional to the local tube pressure, including the vent pressure distribution, P_n , so the absolute pressure level prevailing in the cannon is not a dominant factor. Similarly, the Mach number at the brake entrance affects the load generated by the brake but in a manner similar to the way the muzzle

exit Mach number affects the thrust function in the denominator. This leaves the brake geometry, through the area function, S_n , as the principal determinant of β . For geometrically similar brakes, S_n is directly proportional to the bore area, A , which also appears as a factor in the other terms in the equation, so β should be independent of cannon caliber and only modestly influenced by the ballistics. Calculations for baffle brakes (ref 9) and perforated brakes (ref 19) support this conclusion.

The second parameter of interest is the overpressure ratio, PI, defined as

$$PI = (P_{brk} - P_o) / (P_{brm} - P_o) \quad (5)$$

where the numerator and denominator are the peak free-field overpressures at a given location with and without a brake. As with β , both terms are similar functions of the cannon ballistics, so the ratio should depend only upon brake geometry and, hopefully, be the same for geometrically similar cannons. For baffle brakes, Baur and Schmidt (ref 11) have found that the overpressure scales for cannons of different caliber, but the scaling factor includes some ballistic parameters in addition to the tube diameter. However, they also found that the ratio in Eq. (5) depends only upon the angular location in the field and β , and not upon the scaled distance from the muzzle. The ballistics is a factor only through its more modest effect on β . This is explored below for perforated brakes.

The principal virtue of using these parameters to characterize brake performance is that information obtained with one type of ammunition or one caliber cannon can be used to predict performance in another circumstance. Of course, this must always be tested when data become available, as in the present case.

VELOCITY AND IMPULSE DATA

In the laboratory experiment, the weapon impulse and projectile velocity were measured for each shot. The data are tabulated in Appendix C and summarized in Table 2. Each value is the average of six or more rounds.

Table 2. Summary of Brake Data

Extension	Velocity (m/sec)	Impulse (nt-sec)	Vent Area Ratio	β (%)
bare muzzle	1059.1	150.4	-	-
120-mm standard	1059.5	126.5	3.679	51.1
120-mm modified	1056.4	124.3	3.679	55.9
120-mm side vent	1059.1	125.6	3.679	53.0
105-mm standard	1059.7	121.4	4.777	62.1
105-mm elliptic	1061.9	122.9	4.777	58.9

Since each extension was the same length, the velocities for the brakes should be lower than the bare muzzle value because less work can be done on the projectile by the gas as it expands to lower pressures in the vented region. This pattern is not strictly followed in Table 2, possibly because the round-

to-round deviation, found to be plus or minus 10 m/sec (see Table C3 in Appendix C), exceeds the small variations between brakes. The velocity loss due to venting would appear to be modest.

The vent area ratio, defined as the ratio of the total vent flow area to cannon bore area, has been found to be the dominant factor affecting perforated brake efficiency (refs 12-15,19). The data in the last two columns of Table 2 are consistent with this observation. Turning the flow an additional ten degrees with the 120-mm modified brake increased the efficiency, as expected. Somewhat surprising, however, is the increase in efficiency produced by the side vent design and the decrease found with the elliptic design since both had the same vent area ratio as their standard counterparts.

Plostins and Clay (ref 1) and Gast (ref 3) fired the M490 round from 105-mm cannons having a brake geometrically similar to the 105-mm standard brake used here. The principal difference between the two field experiments was in the measurement of impulse. Plostins and Clay determined impulse indirectly from an analysis of the recoil cylinder pressure and cannon displacement histories. Gast measured the weapon impulse directly at the trunnions with a load cell arrangement. Their results are given in Table 3.

Table 3. Field Experiment Data

Cannon	L_{w0} (knt-sec)	L_w (knt-sec)	$L_{w0} - L_w$ (knt-sec)	β (%)
Plostins and Clay (M490, tube 3)	23.0	15.6	7.4	67.0
code prediction	19.7	15.0	4.7	59.7
Gast (M490, 144 vents)	19.8	15.8	4.0	51.7
code prediction	19.8	15.1	4.7	60.2

For comparison, predictions from an impulse code (ref 19) are also listed in Table 3. The ballistic input for the code was taken from Table 4 of Reference 1. The cannon used by Gast was a few calibers longer than that used by Plostins and Clay, which is why there is a set of predictions for each experiment. The longer tube produces slightly higher impulses, as would be expected.

The large differences in measured brake impulse in column 3 of Table 3 imply considerable uncertainty as to the loads and stresses generated by the brake. The calculated efficiencies lie between the measured values and are in good agreement with the laboratory measurement of 62.1 percent for the '105-mm standard brake' given in Table 2.

Savick (ref 2) and Savick and Baur (ref 4) used a 120-mm cannon with brakes geometrically similar to those used here and found efficiencies that ranged from 77 to 114 percent, well above the 50 to 55 percent range in Table 2. Since the vent area ratio is significantly less than that of the 105-mm brake, the results seem high. The instrumentation used to determine the weapon impulse was being reviewed as this report was being written.

The following equation was given by Carofano (ref 19) to relate

$$\beta = 0.273 A_R (1 - 0.18 L/D)(1 - 0.14 A_R + 0.01 A_R^2) \quad (6)$$

gasdynamic efficiency to the vent area ratio, A_R , and the vent aspect ratio, L/D , where L is the tube wall thickness and D is the vent diameter. It applies to axisymmetric brakes having circular vents drilled at ninety degrees to the tube axis. For brakes with vents of different diameters, an average value of D is computed from the expression

$$D = \frac{\sum_{n=1}^N D_n A_n}{\sum_{n=1}^N A_n} \quad (7)$$

where N is the number of vents, and D_n and A_n are the diameter and area of the n th vent, respectively. Each diameter is weighted by the vent area in the belief that a large vent contributes more to brake performance than a small vent.

Equation (6) is plotted in Figure 2, along with the experimental data for seven of Dillon's 20-mm brakes (ref 12) (see also Table II of Reference 19), the two standard brakes listed in Table 2, and the full-scale 105-mm cannons in Table 3. The plot is interesting because Eq. (6) is actually a fit of computations for a 120-mm cannon (ref 19), yet it compares well with the experimental data for the smaller cannons.

The impulse code (ref 19) is used at Benet to predict the axial and radial load distributions for use as input to a finite element calculation of the stress field in the brake. Based on the discussion above, there seems little reason to question the use of the code for this purpose. What would be desirable is a direct measurement of the transient axial load produced by a brake. Plostins and Clay (ref 1) measured the axial strain but not the circumferential strain. Both are needed to determine the axial load.

THE SHADOWGRAPHS

A shadowgraph was taken for most of the rounds fired. Those for the bare muzzle extension and the 105-mm standard brake are given in Appendix B of Reference 21. The remainder may be found in Appendix B of this report. A few are shown here to aid in the discussion of the free-field overpressure data to be presented below.

As the projectile accelerates in the tube from rest, a shock wave forms ahead of it. The column of air set into motion by the shock is called the precursor flow. The spark light source was triggered, after a preset time delay, by the arrival of the precursor shock at a microphone placed near the muzzle. After passing through the disturbance, the light was diffracted by a large Fresnel lens into the camera.

The discussion begins with a sequence of six shadowgraphs, one of each extension, taken at successively larger time delays. The purpose is to illustrate distinguishing features of the individual brakes as well as the general flow field development.

The shadowgraph in Figure 3 was taken as the projectile base was emerging from the bare muzzle extension. Most of the disturbance in this picture is the precursor flow. Following projectile exit, the propellant gas flow commences and drives the main blast wave which, at this instant, is just starting to form near the muzzle. The solid object below the tube is the trigger microphone. Also visible are the circular striations of the Fresnel lens and a few scratches that can be identified by their repetition in the other shadowgraphs.

The flow field produced by the 120-mm standard brake is shown in Figure 4. The projectile is again just emerging from the muzzle, so the muzzle plume is still primarily precursor air. However, the vent plume is more fully established.

For the 120-mm modified brake in Figure 5, the nose of the projectile is just barely visible in the remnants of the precursor flow at the right. The disturbance is bounded by the precursor shocks formed by the air flowing from the vents and the muzzle. The vent and muzzle plumes generate strong shock waves that can be seen interacting near the muzzle exit plane. The resulting structure is called the main blast wave.

The shadowgraph for the 120-mm side vent design in Figure 6 was taken with the vents placed in the vertical plane. As a result, the flow from the individual vents is discernible. Note that the boundary of the plume upstream of the vents is well separated from the tube. This may also be true of the axisymmetric brakes, but their plumes obscure this feature.

Shadowgraphs of the upstream half of the 105-mm standard and elliptic brakes are shown in Figures 7 and 8, respectively. The semicircular objects at the left are the pressure transducer fixtures at 150 and 165 degrees. The flow from the standard brake, which has twelve vents around the tube circumference, approximates an axisymmetric field in the sense that the shocks from the individual vents have merged to form a single blast wave. The flow field for the elliptic brake, with only six vents around the circumference, remains three-dimensional.

A shadowgraph of the bare muzzle flow field at a later instant is shown in Figure 9. The precursor shock is barely visible. Note that the main blast wave, which intersects the tube just upstream of the transition in diameter, is weakest near the barrel and gets progressively stronger toward the muzzle. This contrasts sharply with the more uniform strength of the main blast wave for the 120-mm standard and modified brakes in Figures 10 and 11. The shock for 120-mm side vent design in Figure 12 appears to be somewhat weaker near the tube, however.

The shadowgraphs in Figures 13 and 14 make an interesting comparison in that the numerous weak waves produced by the elliptic design coalesce near the tube to produce a shock whose strength appears to be comparable to the one produced by the standard brake. The data in the next section quantify these observations.

FREE-FIELD OVERPRESSURE DATA

Seven pressure transducers were used for each shot, placed at angles of 15, 30, 60, 90, 120, 150, and 165 degrees with respect to the line of fire and at a radius of 30 calibers from the muzzle. The pressure histories for the bare muzzle extension and the 105-mm standard brake are given in Appendix B of Reference 21. The remainder may be found in Appendix B of this report.

The peak overpressure data for the main blast wave are summarized in Figure 15 for the 120-mm brakes and Figure 16 for the 105-mm designs. The symbols represent the average peak value of the information in Appendix B. The minimum and maximum values are indicated by the flags in those cases where the data spread exceeds the size of the symbol. The principal effect of venting is seen to be the generation of a more uniform blast field around the cannon. The disturbance is diminished somewhat downstream of the muzzle but considerably strengthened upstream.

To make the comparison easier, all of the brake data are replotted in Figure 17. The ordinate represents the increase in overpressure relative to the bare muzzle case, expressed in decibels, or

$$\text{decibel increase} = 20 \log_{10}[(P_{brk} - P_o)/(P_{brm} - P_o)] \quad (8)$$

The quantity in brackets is simply the overpressure ratio defined by Eq. (5). The decibel scale is used because it is a universally accepted way of measuring blast. The efficiencies are also reproduced in the figure following the brake name.

The comparison in Figure 17a shows that raking the vents back by ten degrees increased the blast levels upstream slightly, which is usually the price paid for an improvement in efficiency. The side vent design in Figure 17b produced an even more pronounced increase, but this is due more to the fact that the transducers were located in the same plane as the vents than to the small improvement in efficiency. The slight decrease at the 165-degree location is consistent with the appearance of the shock in the shadowgraph of Figure 12. Baur and Schmidt (ref 11) found similar results when they compared the pressure distributions around three-dimensional and equivalent axisymmetric versions of baffle brakes when the gages were in the plane of the vents.

The results in Figure 17c show that the elliptic design produced lower blast levels than the standard brake, except near the tube. This is consistent with the shadowgraph in Figure 14 which shows that the flow field for the elliptic brake consists of several weak shocks that coalesce near the tube to produce a strong shock. With comparable shock strengths near the tube and lower efficiency, there is no incentive to use this design in place of the standard brake.

The two standard brakes are compared in Figure 17d. This makes sense only because both are 20-mm models. The 105-mm design, having the larger vent area ratio, produced somewhat higher blast levels. Perhaps the difference would have been greater, commensurate the improvement in efficiency, if the vents in the 120-mm brake were located at the muzzle instead of farther upstream (see Figure 1).

The laboratory results are compared with the 105-mm field data in Figure 18 and the 120-mm data in Figure 19. The bare muzzle data reported by Plostins and Clay (ref 1) were used to construct Figure 18. These authors did not report overpressure data for the particular 105-mm brake configuration discussed here.

The field data show good agreement with each other, particularly since the individual rounds are ballistically quite different. This supports the use of the overpressure ratio as a scaling parameter. However, the 20-mm data fall below the full-scale results at the upstream locations for all but the 120-mm side vent design. This suggests that there may be a ground effect present in the field experiments. For the axisymmetric brakes, the gas vented toward the ground may be deflected upstream and limit the expansion process in the air compressed by the blast wave. With the side vent design, the ground would not be an inhibiting factor, and the laboratory arrangement would better approximate the field experiments. At this point, rather than conclude that the laboratory experiments are a poor simulation of field experiments or that the overpressure ratio is an inadequate scaling parameter, a 20-mm program should be conducted that includes tests with and without a ground plane. Both the shadowgraph and pressure data would be helpful in assessing its importance.

CONCLUSIONS

The gasdynamic efficiencies measured in the laboratory show good agreement with previous 20-mm results, fair agreement with the 105-mm experiments, and poor agreement with the 120-mm results. An instrumentation problem is suspected in the latter case. The results also compare well with predictions obtained from the impulse code (ref 19) used at Benet to design perforated brakes. There seems little

reason to question the use of the code for this purpose. What would be desirable is a direct measurement of the transient axial load produced by a brake.

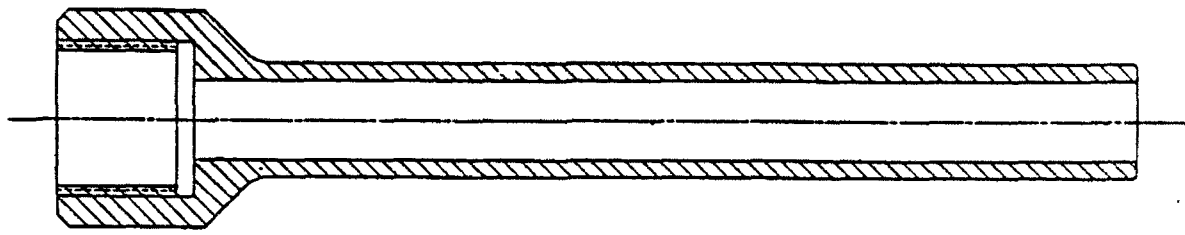
The field data for the different rounds scaled well using the overpressure parameter. However, the 20-mm data fall below the full-scale results at the upstream locations for all but the 120-mm side vent design. This suggests that there may be a ground effect present in the field experiments. A 20-mm program that includes tests with and without a ground plane would be helpful in assessing its importance.

REFERENCES

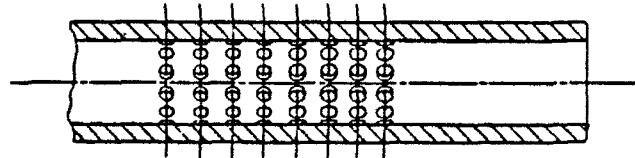
1. P. Plostins and W.H. Clay, "Performance of Lightweight 105-mm Cannon Designs" (U), Technical Report BRL-TR-2749, Ballistic Research Laboratory, Aberdeen Proving Grounds, MD, July 1986.
2. D. Savick, Ballistic Research Laboratory, Aberdeen Proving Grounds, MD, Technical Report in preparation.
3. R.G. Gast, "Determination of Muzzle Brake Efficiency for the EX35 Gun System," Benet Internal Technical Report BITR No. 89-7, Benet Laboratories, Watervliet, NY, November 1989.
4. D. Savick and E. Baur, "The Performance Characteristics for a 120-mm Perforated Muzzle Brake" (U), Technical Report BRL-TR-3816, Ballistic Research Laboratory, Aberdeen, MD, May 1990.
5. D. Savick, Ballistic Research Laboratory, Aberdeen Proving Grounds, MD, Technical Report in preparation.
6. F. Smith, "Model Experiments on Muzzle Brakes," RARDE Report 2/66, Fort Halstead, UK, June 1966.
7. L.L. Pater, "Muzzle Brake Parameter Study," Technical Report NSWC/DL TR-3531, Naval Surface Weapons Laboratory, Dahlgren, VA, October 1976.
8. L.L. Pater, "Scaling of Muzzle Brake Performance and Blast Field," Technical Report NSWC/DL TR-3049, Naval Surface Weapons Laboratory, Dahlgren, VA, October 1974.
9. K.S. Fansler, "A Simple Method for Predicting Muzzle Brake Effectiveness and Baffle-Surface Pressure," Technical Report ARBRL-TR-02335, Ballistic Research Laboratory, Aberdeen, MD, June 1981.
10. K.C. Phan, "An Experimental Study of Model Muzzle Brake Performance," Proceedings of the Third Workshop on Launch Blast Overpressure, Special Publication BRL-SP-66, Ballistic Research Laboratory, Aberdeen, MD, June 1987.
11. E.H. Baur and E.M. Schmidt, "Design Optimization Techniques for Muzzle Brakes," Memorandum Report BRL-MR-3504, Ballistic Research Laboratory, Aberdeen, MD, March 1986.
12. R.E. Dillon, Jr., "A Parametric Study of Perforated Muzzle Brakes," Technical Report ARLCB-TR-84015, Benet Weapons Laboratory, Watervliet, NY, May 1984.
13. R.E. Dillon, Jr., "Wall Thickness and Vent Area Effects on Perforated Muzzle Brake Performance," Technical Report ARLCB-TR-84020, Benet Weapons Laboratory, Watervliet, NY, May 1984.
14. R.E. Dillon, Jr. and H.T. Nagamatsu, "An Experimental Study of Perforated Muzzle Brakes," Technical Report ARLCB-TR-84004, Benet Weapons Laboratory, Watervliet, NY, February 1984.
15. R.E. Dillon, Jr. and H.T. Nagamatsu, "An Experimental Study of Perforated Muzzle Brakes," AIAA Paper 84-1642, presented at the AIAA 17th Fluid Dynamics, Plasma Dynamics, and Lasers Conference, Snowmass, Colorado, 25-27 June 1984.

16. H.T. Nagamatsu, K.Y. Choi, and R.E. Duffy, "Wall Thickness and Flow Mach Number Effects on Pressure Distribution in the Vent Hole for Perforated Muzzle Brakes," ARDEC Contractor Report ARCCB-CR-86038, Rensselaer Polytechnic Institute, Troy, NY, November 1986.
17. R.E. Dillon, Jr. and H.T. Nagamatsu, "A Method of Analyzing Perforated Muzzle Brake Performance," Technical Report ARLCB-TR-84002, Benet Weapons Laboratory, Watervliet, NY, February 1984.
18. H.T. Nagamatsu, K.Y. Choi, R.E. Duffy, and G.C. Carofano, "An Experimental and Numerical Study of the Flow Through a Vent Hole in a Perforated Muzzle Brake," Technical Report ARCCB-TR-87016, Benet Laboratories, Watervliet, NY, June 1987.
19. G.C. Carofano, "The Gasdynamics of Perforated Muzzle Brakes," Technical Report ARCCB-TR-88006, Benet Laboratories, Watervliet, NY, February 1988.
20. M.J. Glennon, Private Communication, U.S. Army ARDEC, Benet Laboratories, Watervliet, NY.
21. G.C. Carofano, "Blast Field Contouring Using Upstream Venting," Technical Report ARCCB-TR-93009, Benet Laboratories, Watervliet, NY, March 1993.
22. G.C. Carofano, "The Blast Field Produced by a Cannon Having a Perforated Muzzle Brake," Technical Report ARCCB-TR-88043, Benet Laboratories, Watervliet, NY, December 1988.
23. G.C. Carofano, "A Comparison of Experimental and Numerical Blast Data for Perforated Muzzle Brakes," Technical Report ARCCB-TR-90034, Benet Laboratories, Watervliet, NY, December 1990.

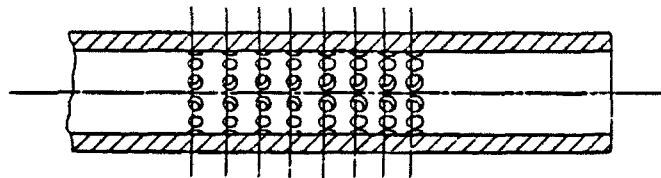
(a) bare muzzle extension



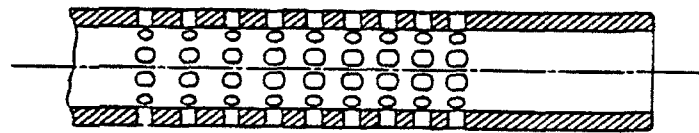
(b) 120-mm standard brake



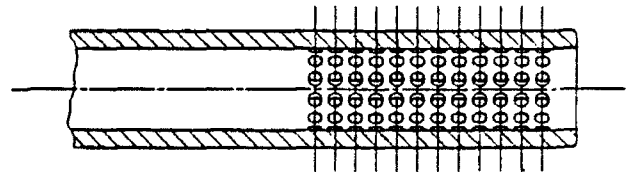
(c) 120-mm modified brake



(d) 120-mm side vent brake



(e) 105-mm standard brake



(f) 105-mm elliptic brake

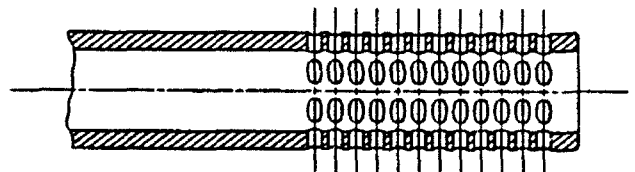


Figure 1. Sketch of the six extensions used in the experiments.

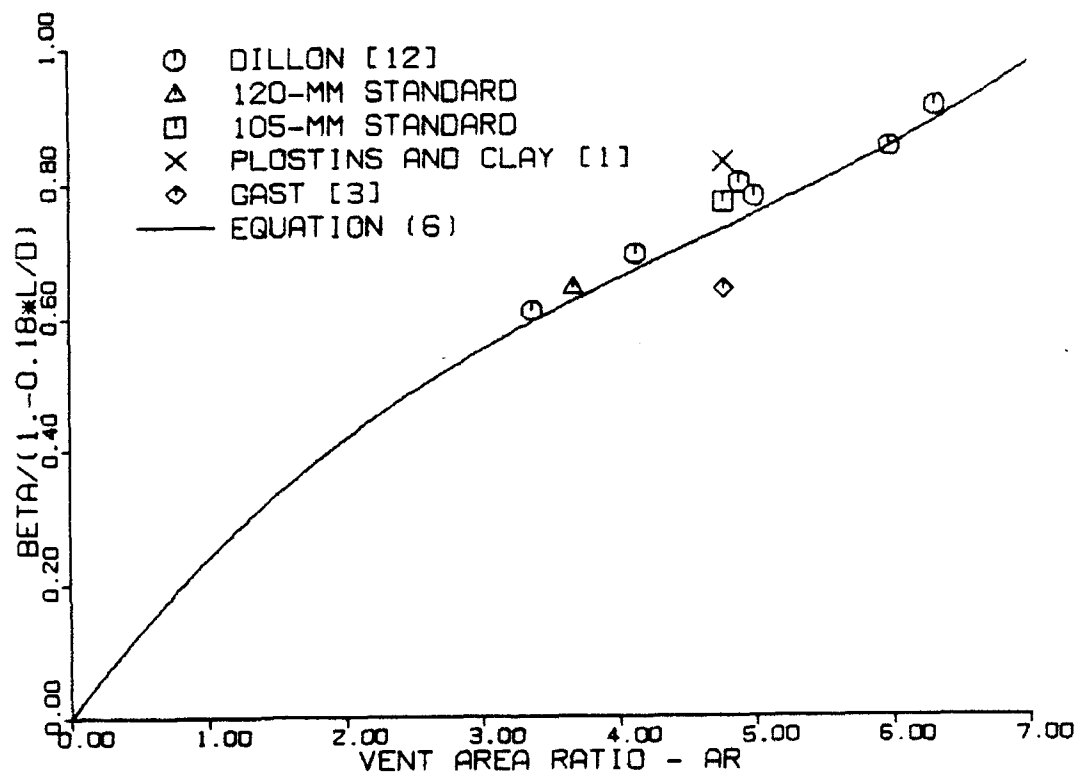


Figure 2. Comparison of Eq. (6) with the experimental data.



Figure 3. Shadowgraph of the bare muzzle flow field taken with no time delay
(round 19531, Appendix B of Reference 21).



Figure 4. Shadowgraph of the 120-mm standard brake flow field taken with a 75-microsecond time delay (round 19535, Appendix B).

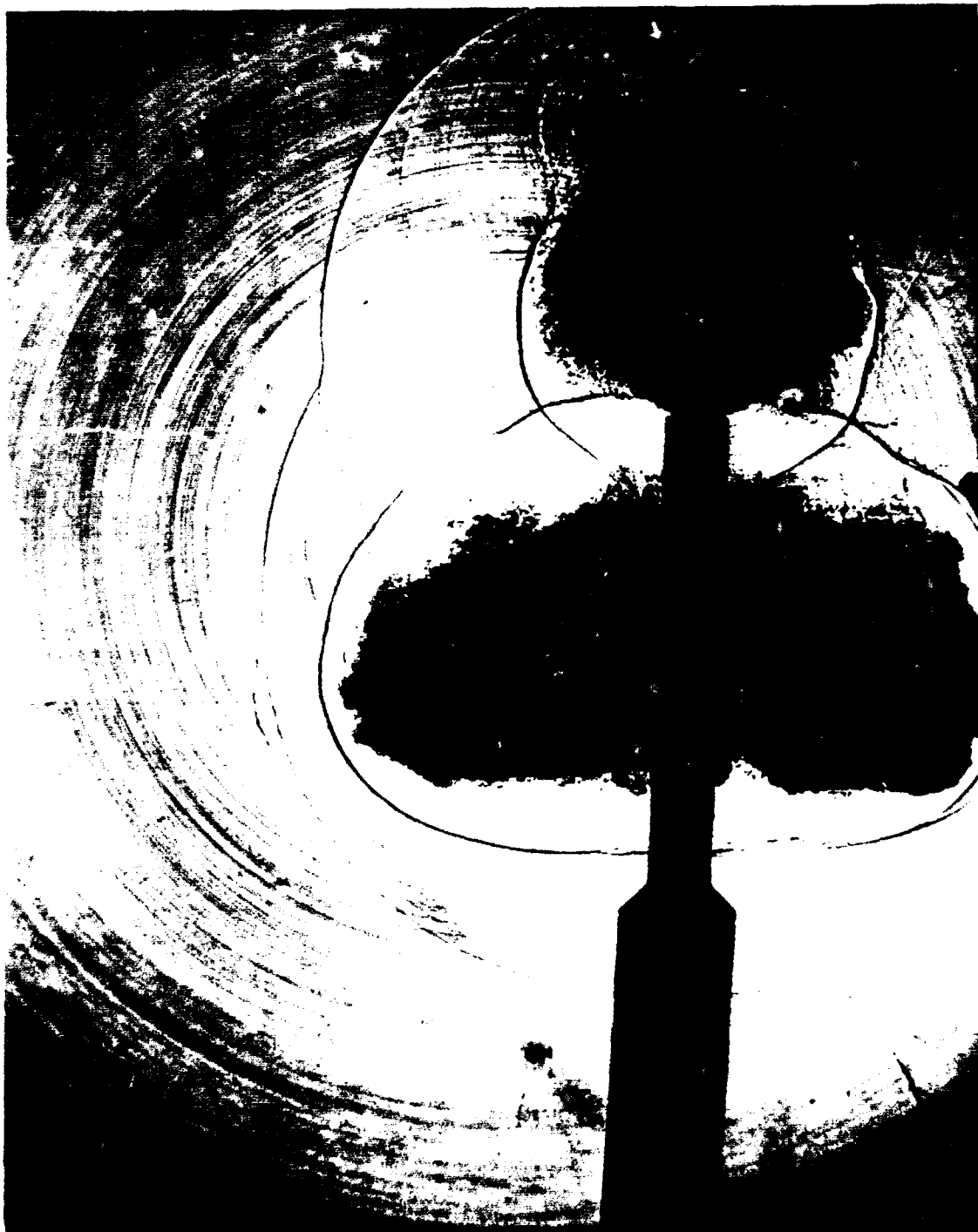


Figure 5. Shadowgraph of the 120-mm modified brake flow field taken with a 150-microsecond time delay (round 19538, Appendix B).



Figure 6. Shadowgraph of the 120-mm side vent brake flow field taken with a 300-microsecond time delay (round 19542, Appendix B).

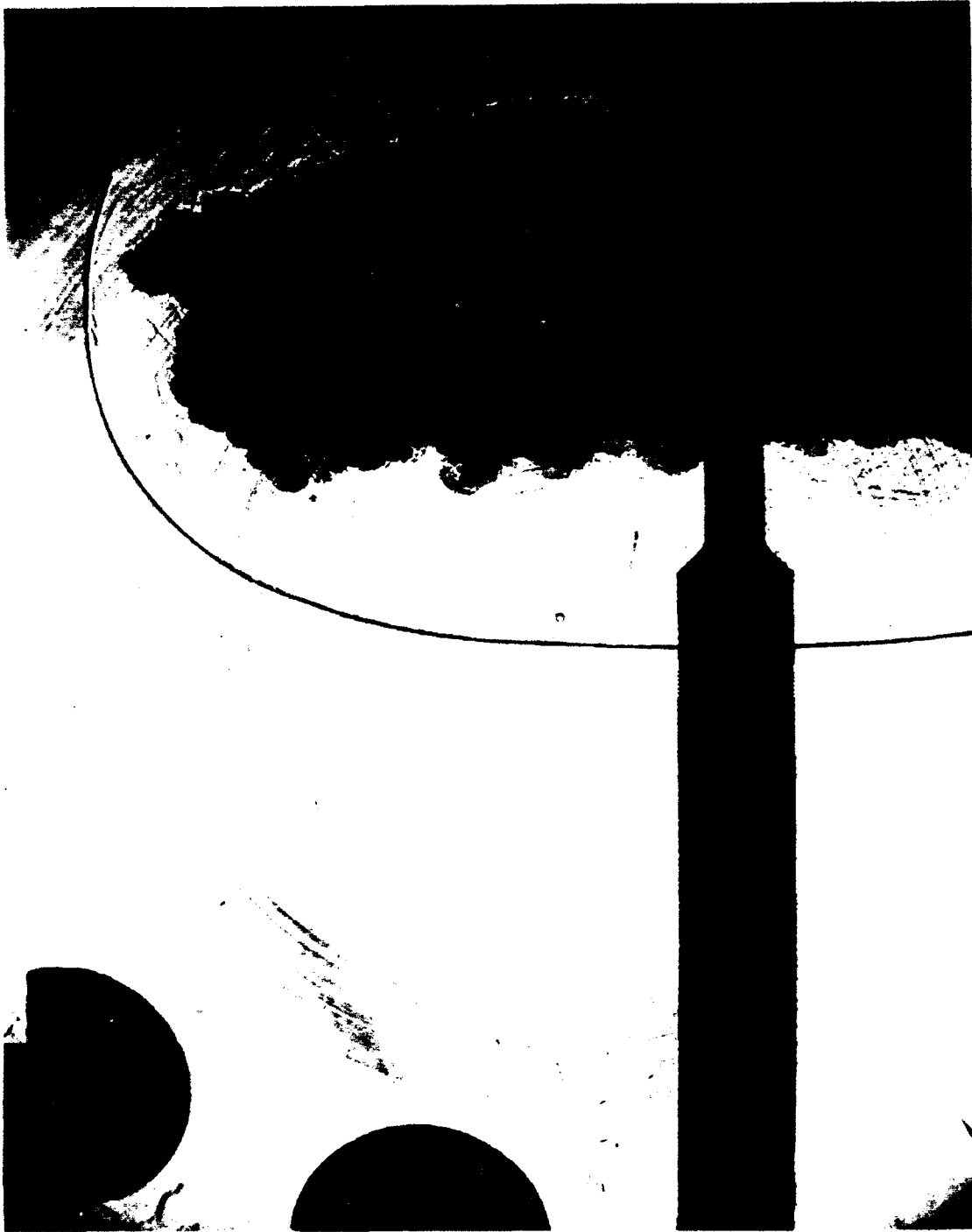


Figure 7. Shadowgraph of the 105-mm standard brake flow field taken with a 450-microsecond time delay (round 19566, Appendix B of Reference 21).



Figure 8. Shadowgraph of the 105-mm elliptic brake flow field taken with a 450-microsecond time delay
(round 19570, Appendix B).



Figure 9. Shadowgraph of the bare muzzle flow field taken with a 750-microsecond time delay
(round 19556, Appendix B of Reference 21).



Figure 10. Shadowgraph of the 120-mm standard brake flow field taken with a 750-microsecond time delay (round 19559, Appendix B).



Figure 11. Shadowgraph of the 120-mm modified brake flow field taken with a 750-microsecond time delay (round 19562, Appendix B).



Figure 12. Shadowgraph of the 120-mm side vent brake flow field taken with a 750-microsecond time delay ~
(round 19565, Appendix B).



Figure 13. Shadowgraph of the 105-mm standard brake flow field taken with a 750-microsecond time delay (round 19569, Appendix B of Reference 21).



Figure 14. Shadowgraph of the 105-mm elliptic brake flow field taken with a 750-microsecond time delay
(round 19572, Appendix B).

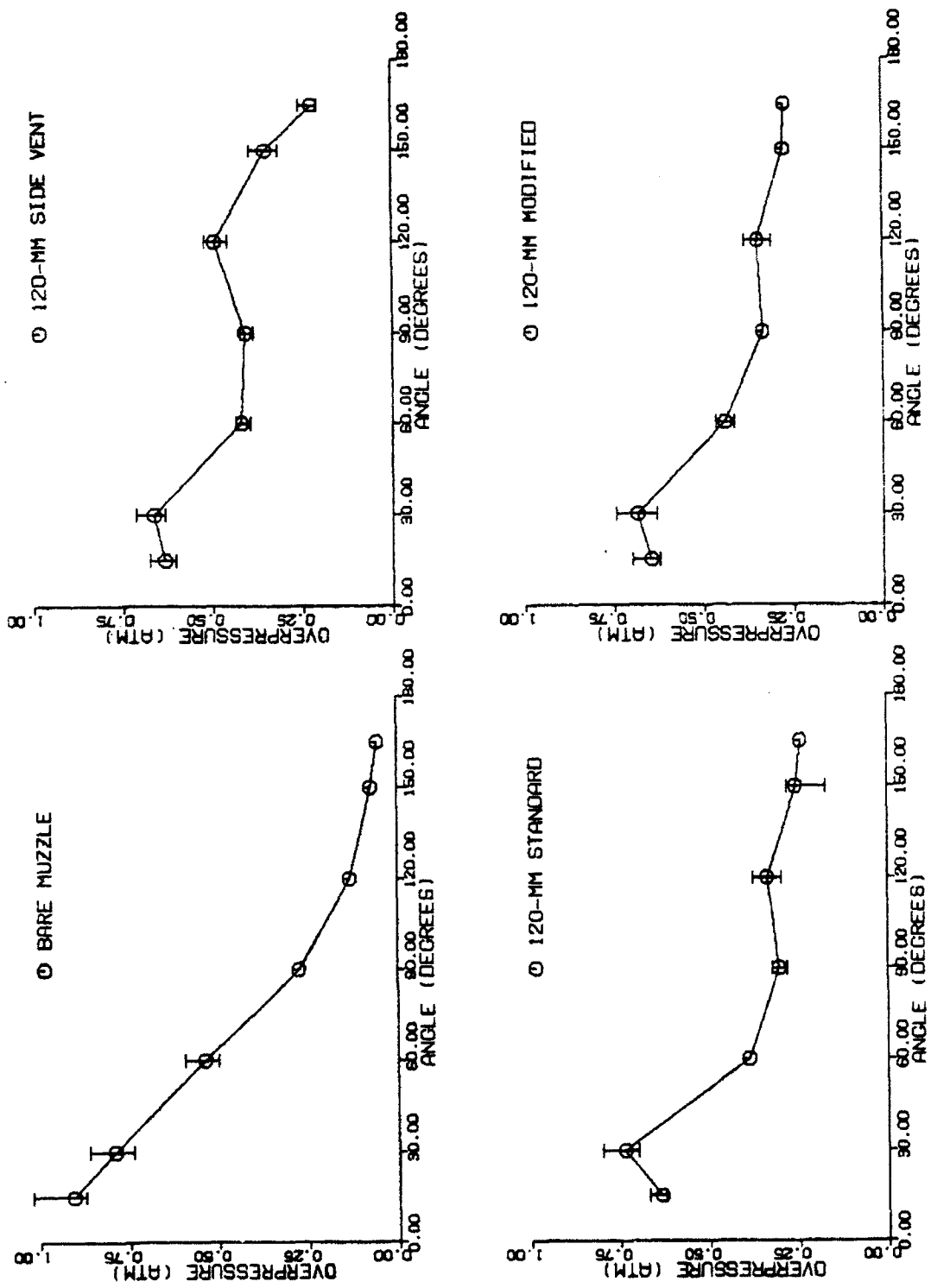


Figure 15. Summary of experimental overpressure data for the bare muzzle case and the 120-mm model brakes.

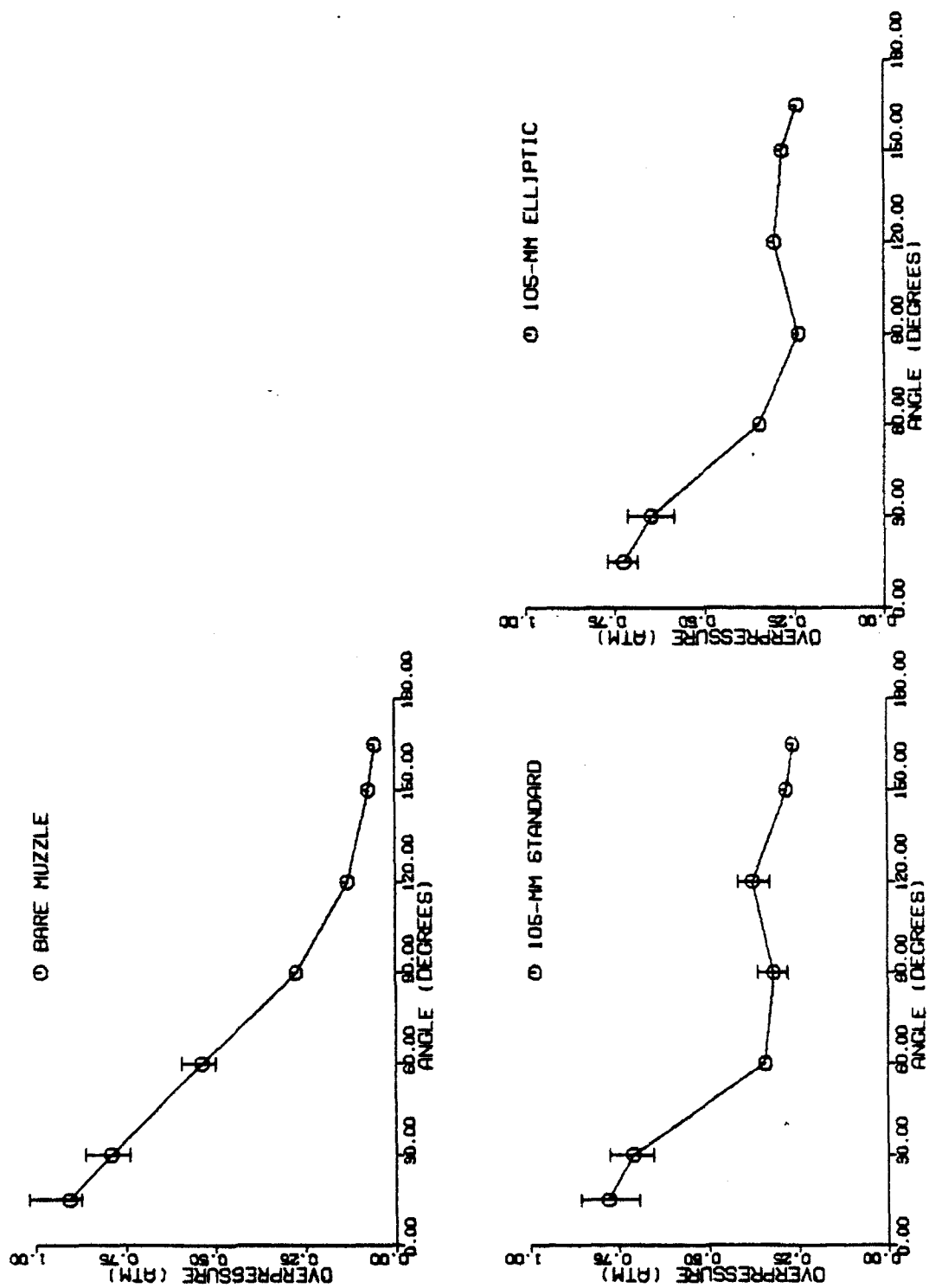


Figure 16. Summary of experimental overpressure data for the bare muzzle case and the 105-mm model brakes.

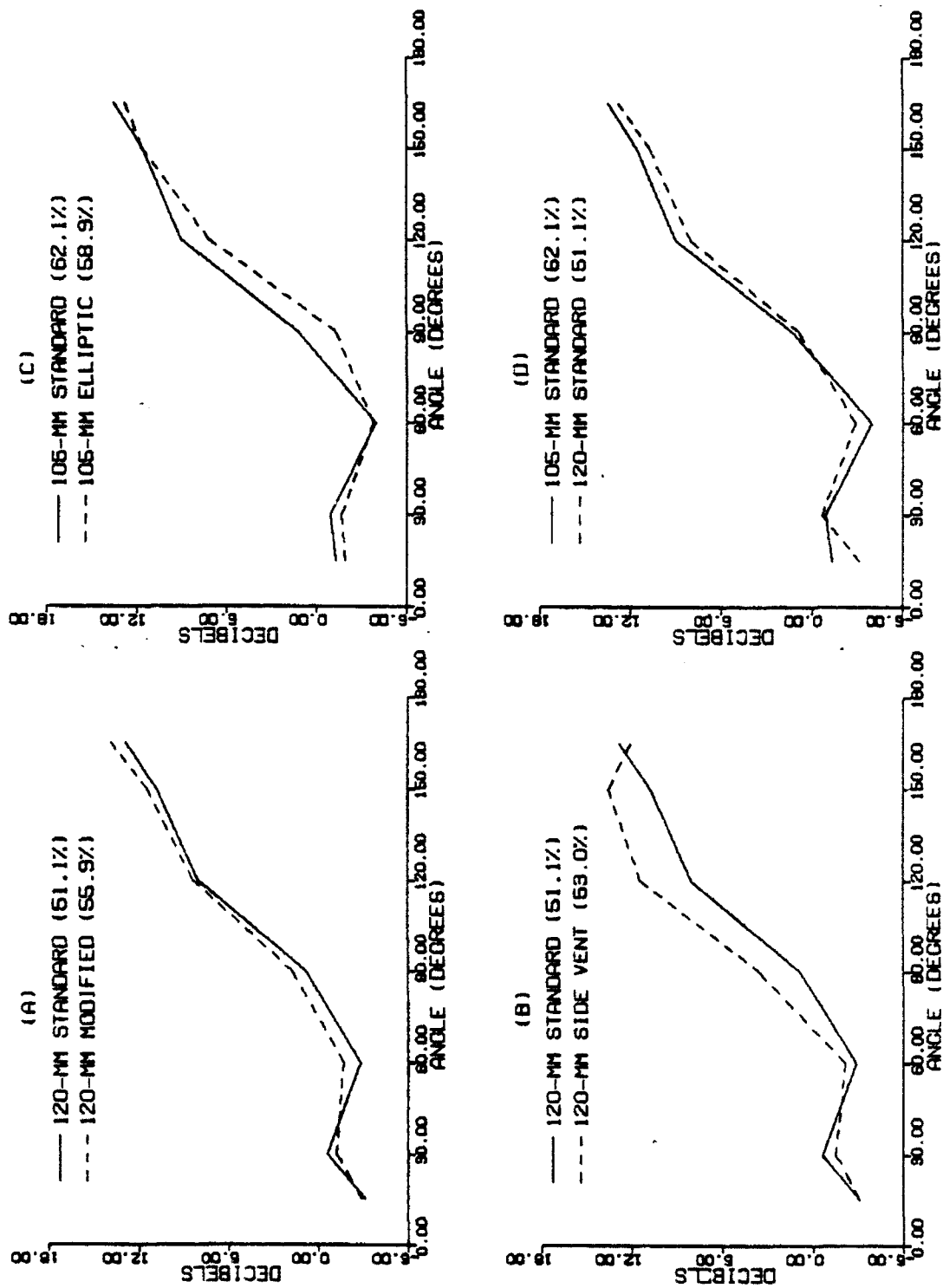


Figure 17. Comparison of experimental overpressure data, measured in decibels, for all of the model brakes.

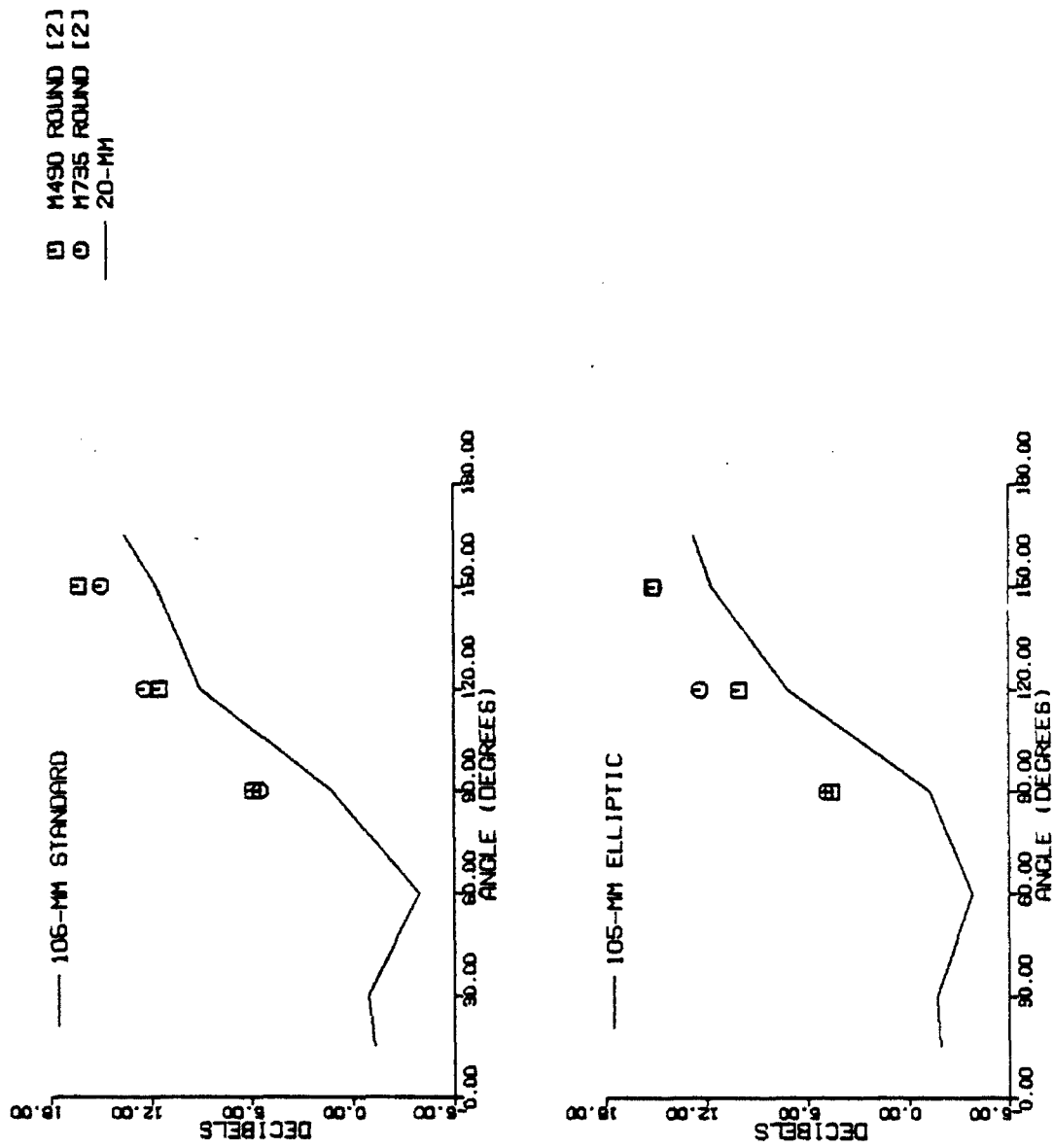


Figure 18. Comparison of experimental overpressure data for the 105-mm model and full-scale experiments.

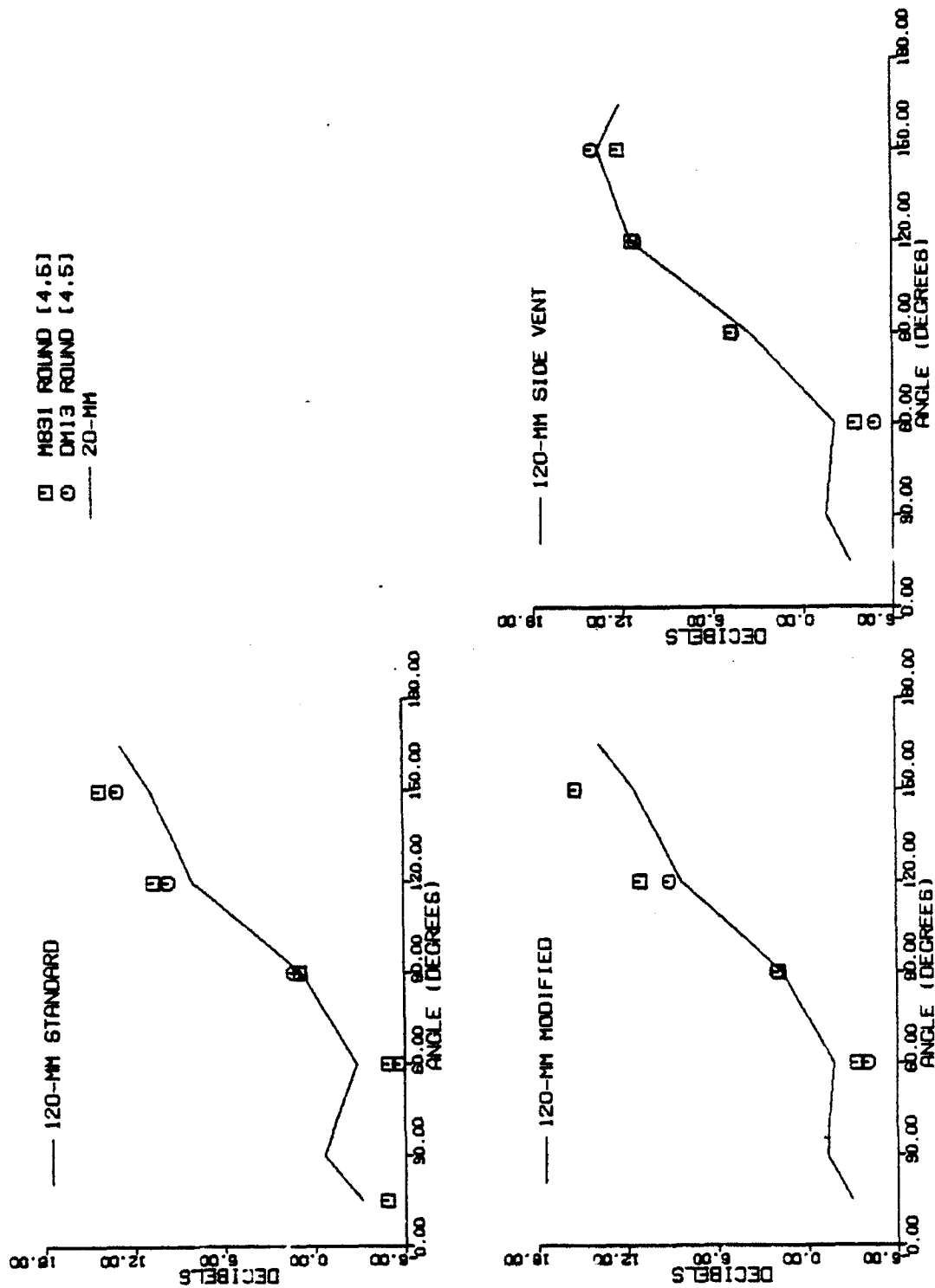


Figure 19. Comparison of experimental overpressure data for the 120-mm model and full-scale experiments.

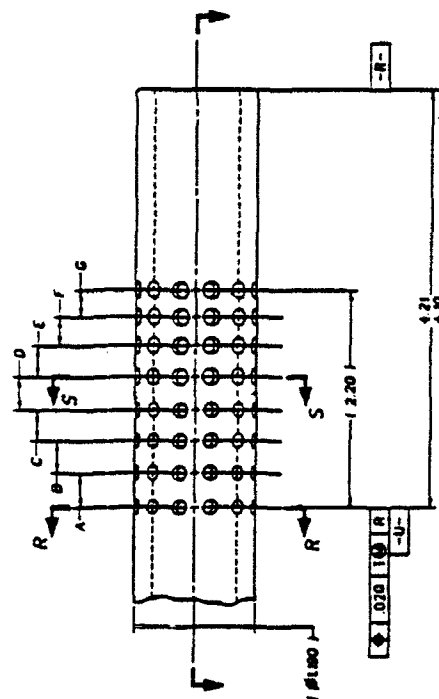
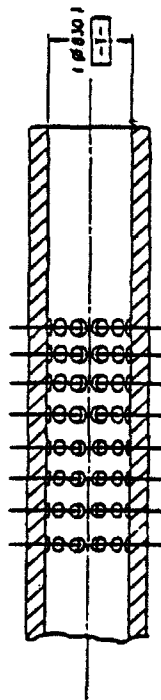
APPENDIX A

This appendix contains scaled drawings of the six extensions used in the experiments. Note that the dimensions are in English units, not metric units as used elsewhere in this report. Each extension was the same length.

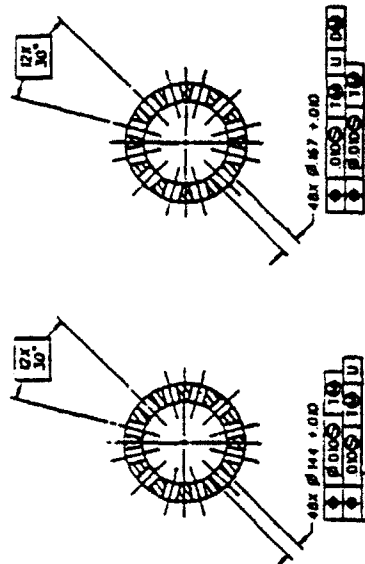
Figure A1. Scaled drawing of the bare muzzle extension.

CENTER TO CENTER
AXIAL SPACING OF HOLES

A	.318
B	.328
C	.309
D	.318
E	.318
F	.289
G	.270



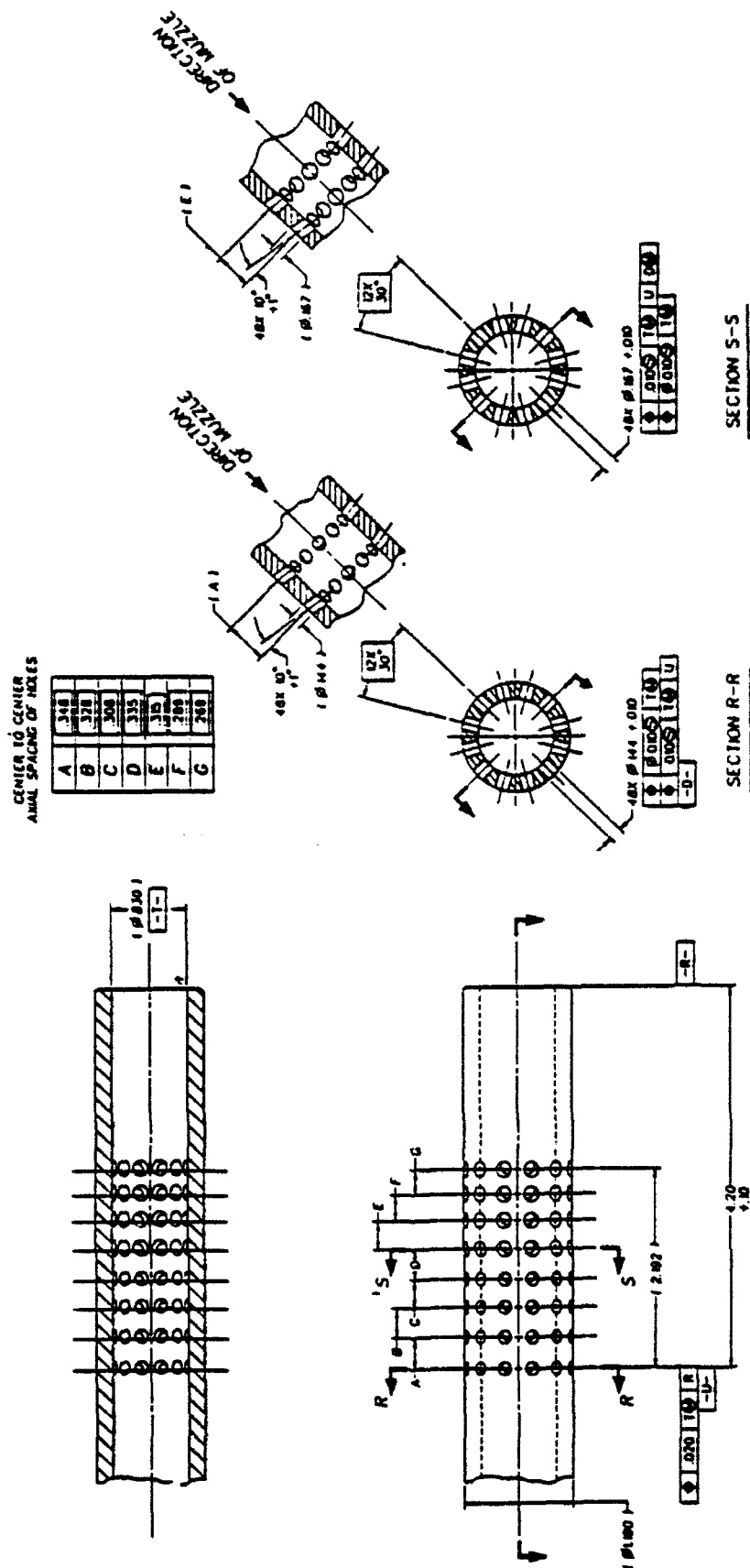
NOTE:
1. THE NOZZLE END HOLE PATTERN CONSISTS OF 2 SETS OF HOLES.
THE FIRST 4 ROWS FROM THE NOZZLE END ARE (1/8) INCH HOLES.
THE NEXT 4 ROWS ARE (1/8) INCH HOLES.
2. BREAK EDGES AT ID AND OD FOR ALL HOLES .010 MAX.



SECTION S-S

SECTION R-R

Figure A2. Scaled drawing of the 120-mm standard brake.



- NOTE:
1. THE MUZZLE END HOLE PATTERN CONSISTS OF 2 SETS OF HOLES. THE FIRST FOUR ROWS FROM THE MUZZLE END ARE 1.0100 HOLES. THE NEXT FOUR ROWS ARE 1.0100 HOLES.
 2. BREAK EDGES AT 1.0 AND 1.20 FOR ALL HOLES 1.0100 MAX.

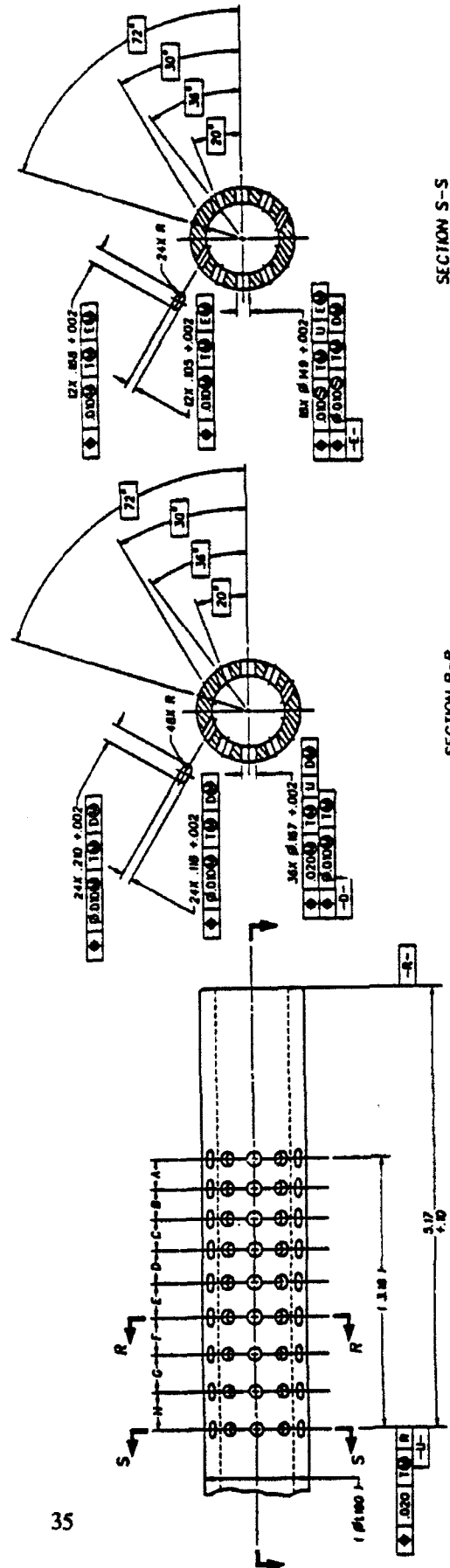
Figure A3. Scaled drawing of the 120-mm modified brake.

CENTER TO CENTER
AXIAL SPACING OF HOLES

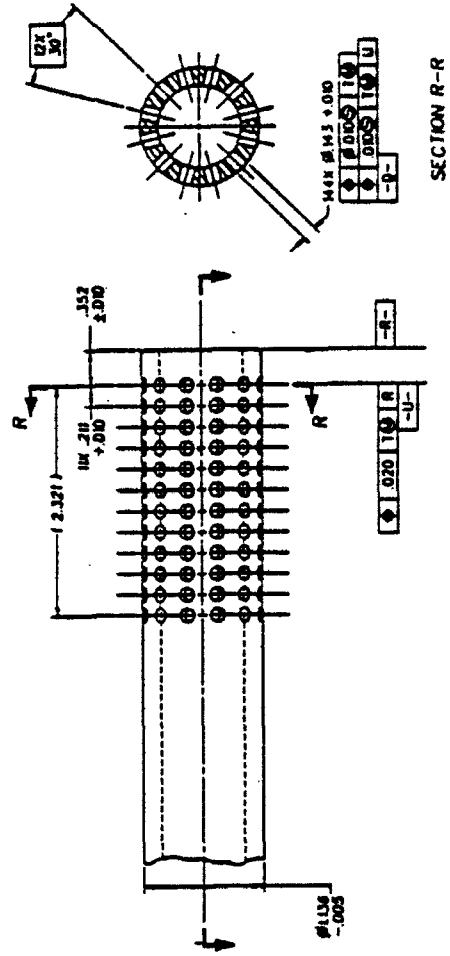
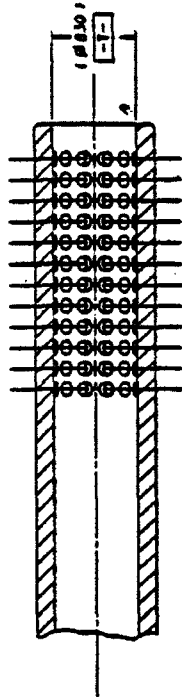
A	348
B	354
C	361
D	367
E	405
F	435
G	440
H	446



35



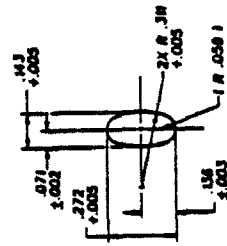
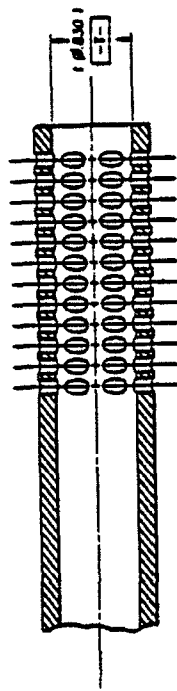
A4. Scaled drawing of the 120-mm side vent brake.



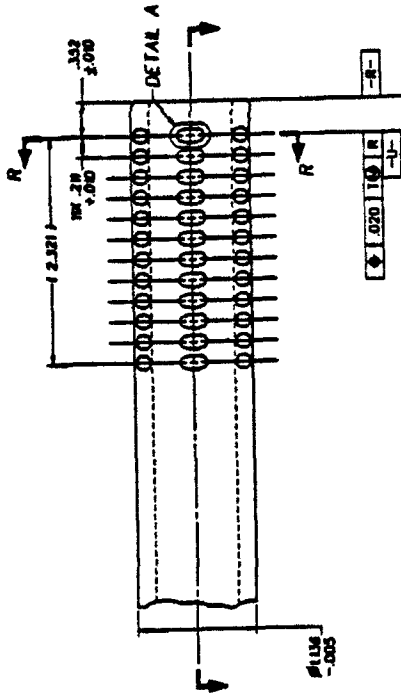
NOTE:

1 BREAK EDGES AT ID AND O.D. FOR ALL HOLES .010 MAX.

A5. Scaled drawing of the 105-mm standard brake.



DETAIL A
SCALE 4/1



SECTION R-R

NOTE:
1. BREAK EDGES AT I.D. AND O.D. FOR ALL HOLES .010 MAX.

A6. Scaled drawing of the 105-mm elliptic brake.

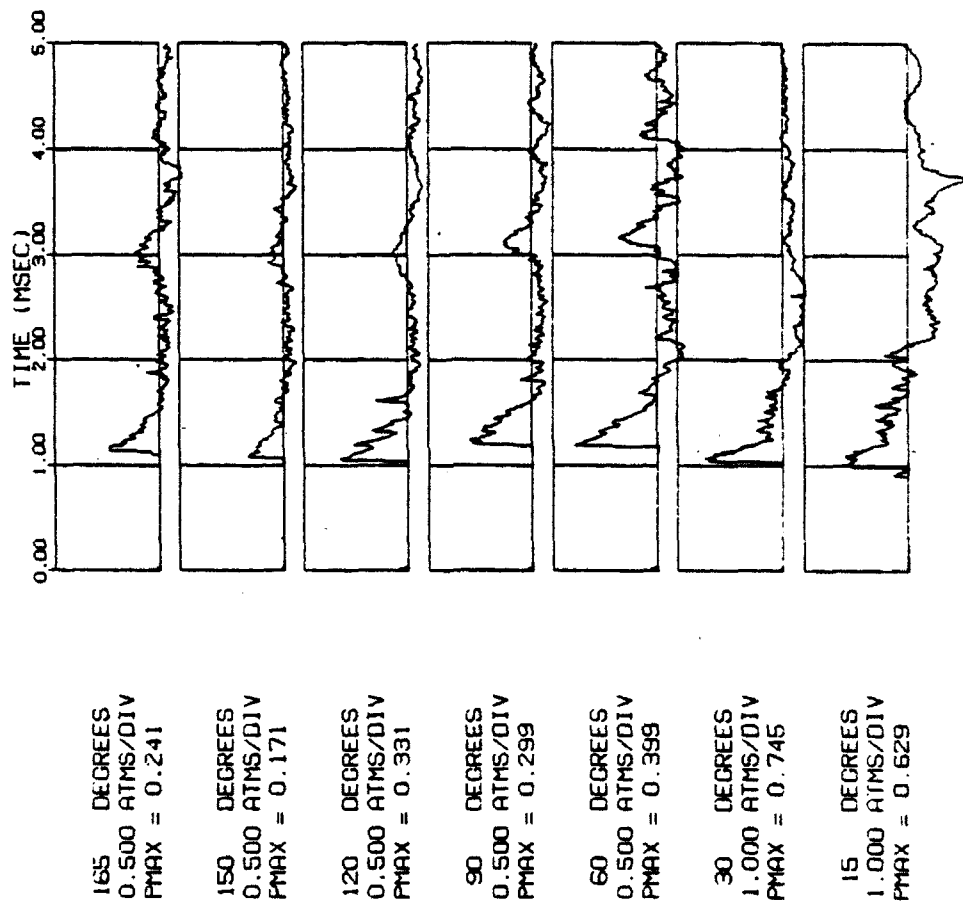
APPENDIX B

The data presented in this appendix were obtained in conjunction with a blast reduction study reported elsewhere (ref 21). Fifty-nine rounds were fired in the program, forty-nine of which pertain to this study. The remaining ten rounds refer to a special brake with a split vent pattern. The pressure histories and shadowgraphs for the bare muzzle case and the 105-mm standard brake are given in Appendix B of Reference 21 and are not repeated here.

For each round, a set of pressure histories is given on the left-hand page, and the corresponding shadowgraph is given on the right-hand page. In some cases, data at one or more of the transducer locations is missing, in others, the shadowgraph is missing. When constructing the overpressure plots in Figures 24 through 28 of the report, only those rounds for which data were available at every transducer location were used. To avoid confusion, the data used in the report is specified in the figure captions.

Seven pressure histories were recorded for each shot. Zero time corresponds approximately to the instant the projectile leaves the barrel. The ordinate of each sub-grid represents overpressure (pressure above atmospheric pressure) measured in atmospheres. Also indicated are the transducer location and maximum pressure of the main blast wave for each trace.

R534 - 30 CAL - (#2) 120MM 4X4

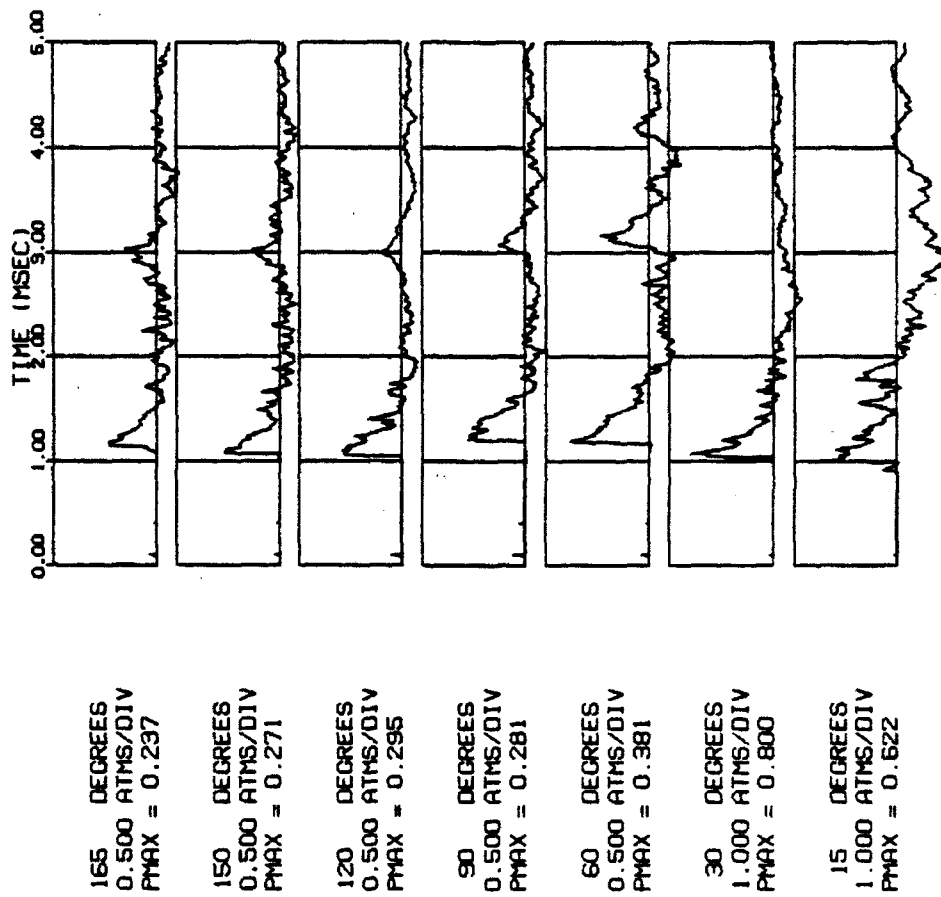


B1a. Pressure histories for round 19534, 120-mm standard brake at 30 calibers. Data used in report figures.



B1b. Shadowgraph for round 19534, 120-mm standard brake, taken with no time delay.

R535 - 30 CAL - (*2) 120MM 4X4

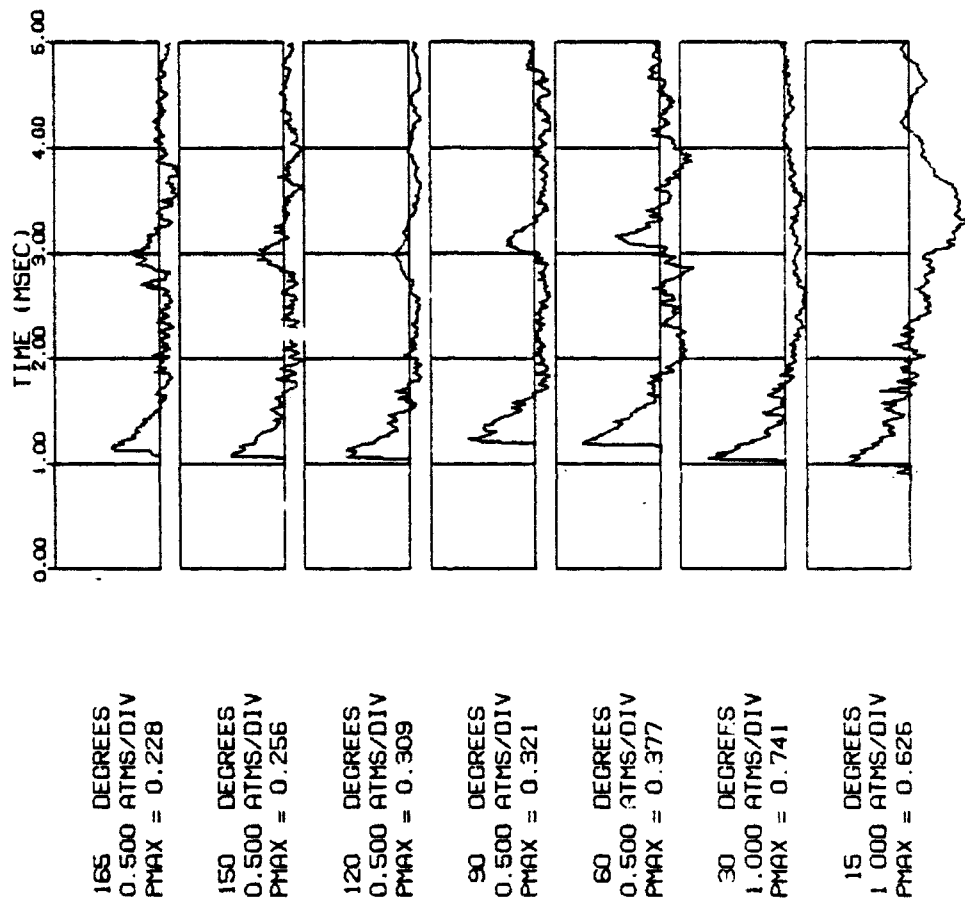


B2a. Pressure histories for round 19535, 120-mm standard brake at 30 calibers. Data used in report figures.



B2b. Shadowgraph for round 19535, 120-mm standard brake, taken with a 75-microsecond time delay.

RS36 - 30 CAL - (#2) 120MM 4X4

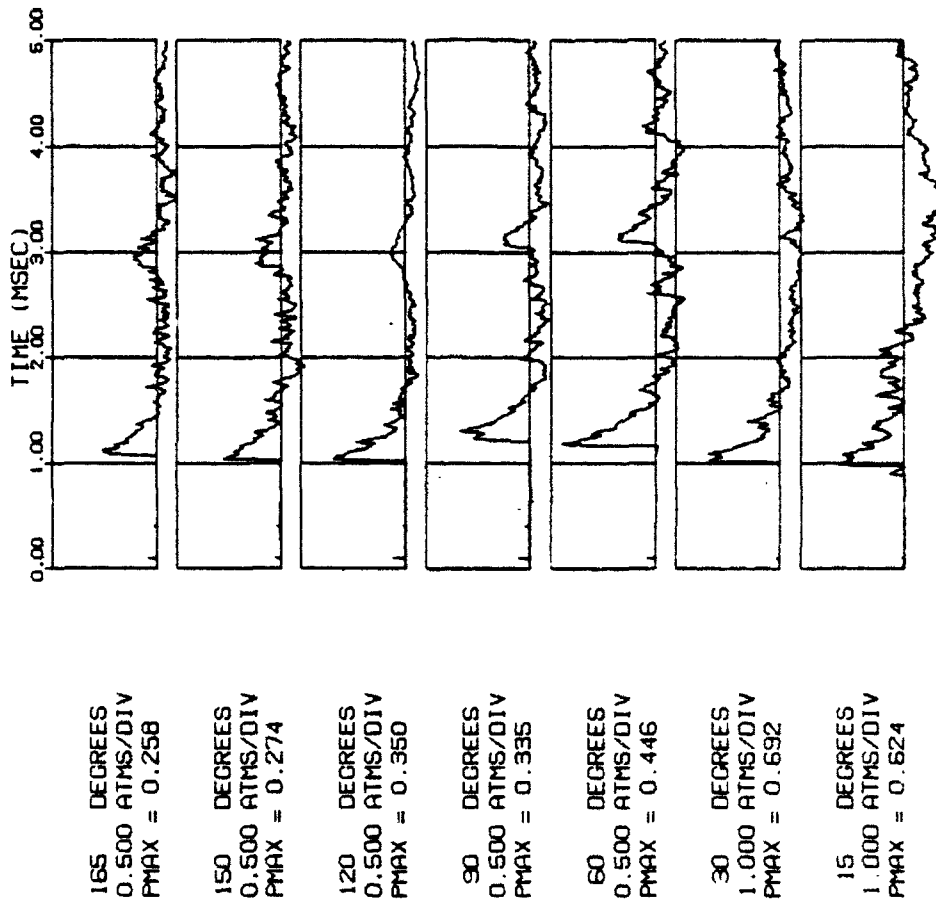


B3a. Pressure histories for round 19536, 120-mm standard brake at 30 calibers. Data used in report figures.



B3b. Shadowgraph for round 19536, 120-mm standard brake, taken with a 300-microsecond time delay.

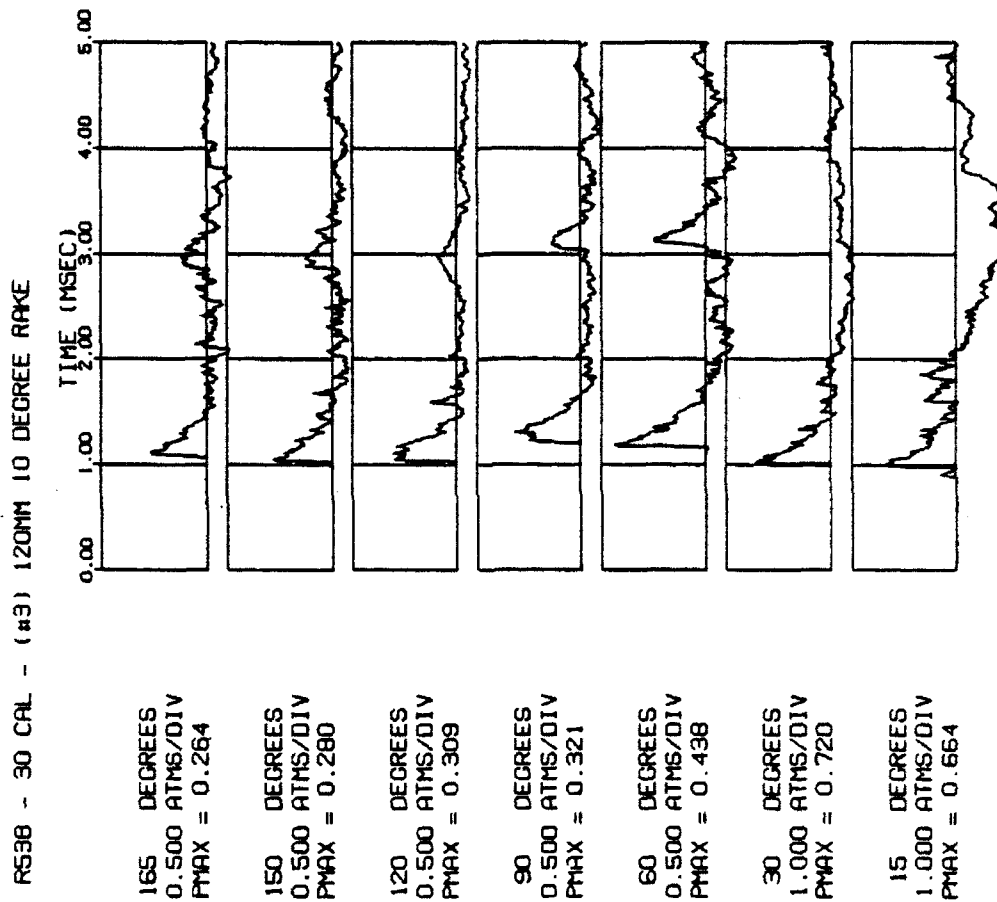
R537 - 30 CAL - (#3) 120MM 10 DEGREE RAKE



B4a. Pressure histories for round 19537, 120-mm modified brake at 30 calibers. Data used in report figures.



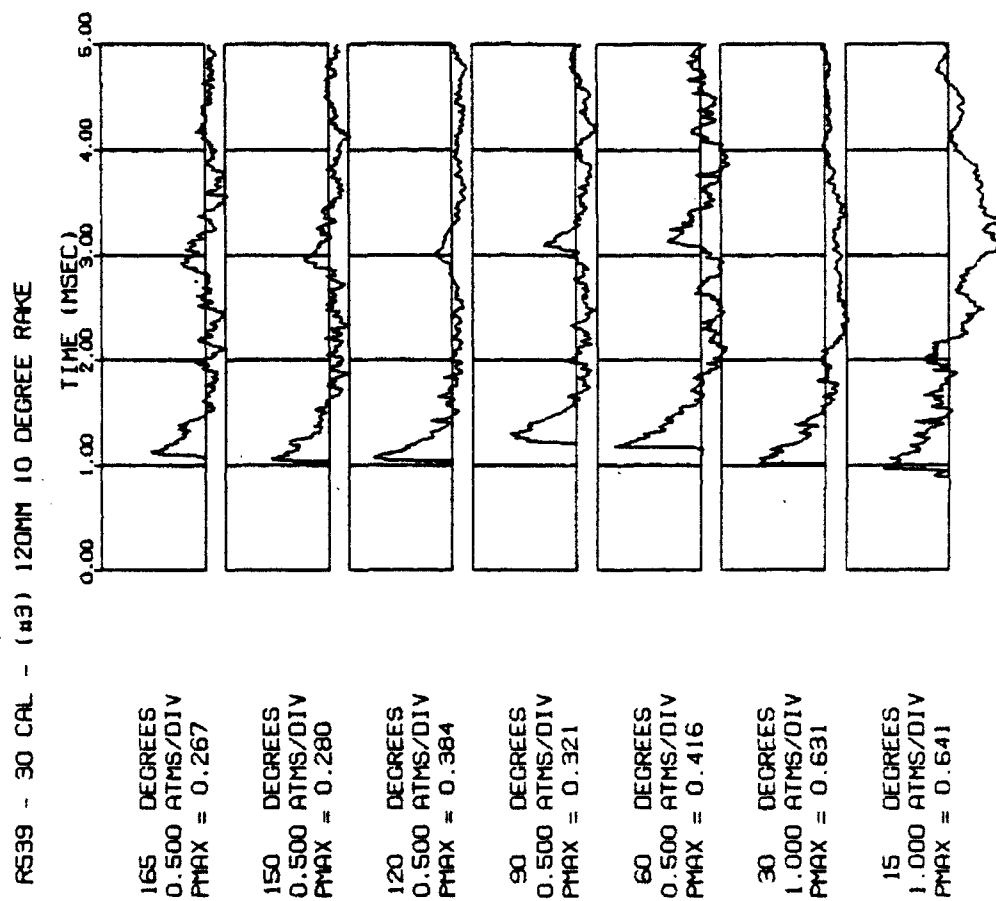
B4b. Shadowgraph for round 19537, 120-mm modified brake, taken with no time delay.



B5a. Pressure histories for round 19538, 120-mm modified brake at 30 calibers. Data used in report figures.



B5b. Shadowgraph for round 19538, 120-nm modified brake, taken with a 150-microsecond time delay.

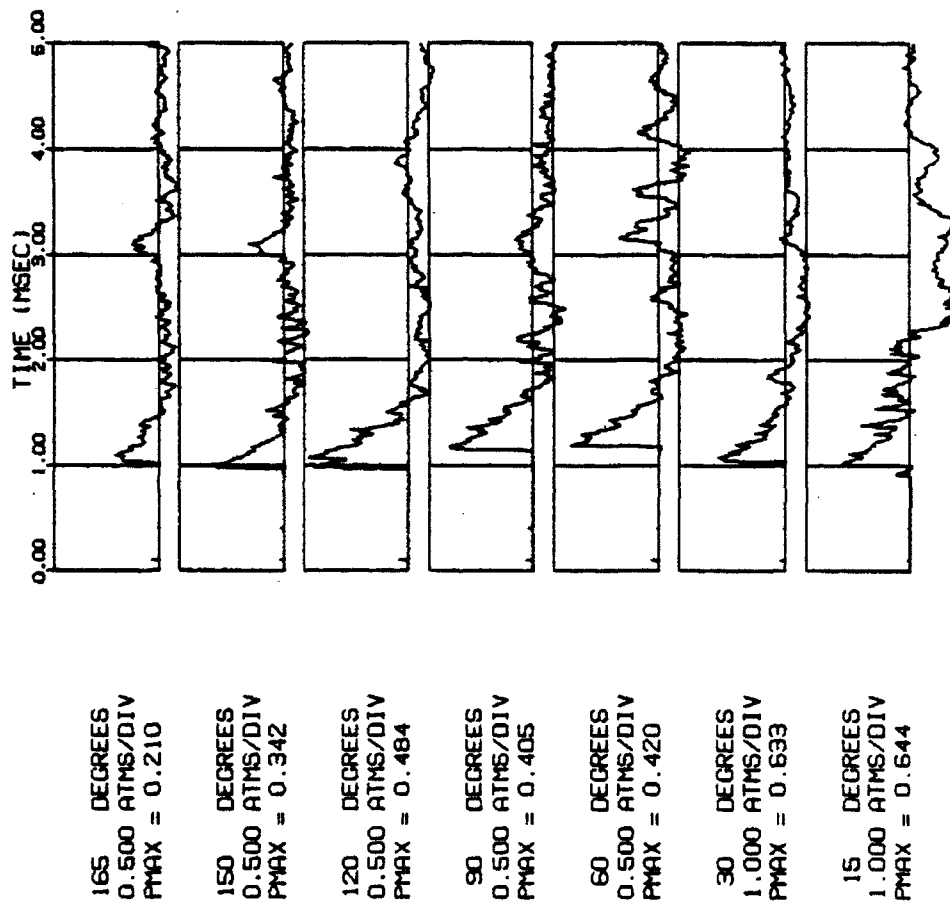


B6a. Pressure histories for round 19539, 120-mm modified brake at 30 calibers. Data used in report figures.



B6b. Shadowgraph for round 19539, 120-mm modified brake, taken with a 300-microsecond time delay.

RS40 - 30 CAL - (#4) 120MM SIDE VENTS

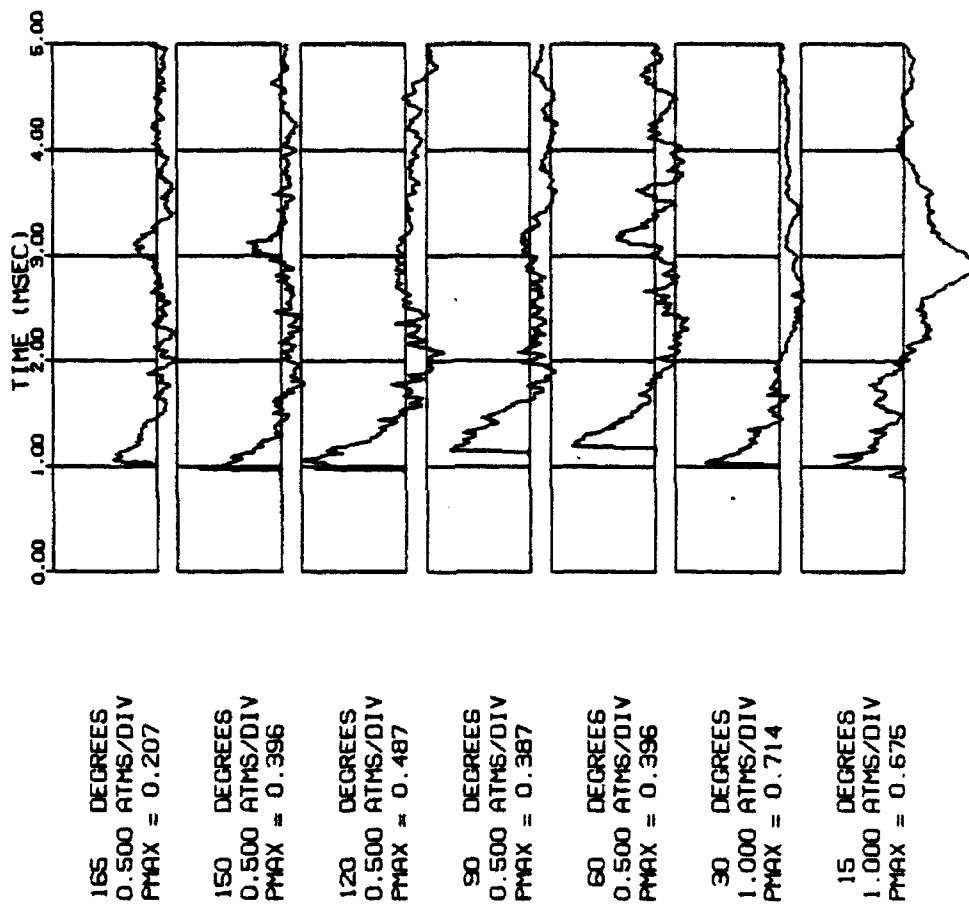


B7a. Pressure histories for round 19540, 120-mm side vent brake at 30 calibers. Data used in report figures.

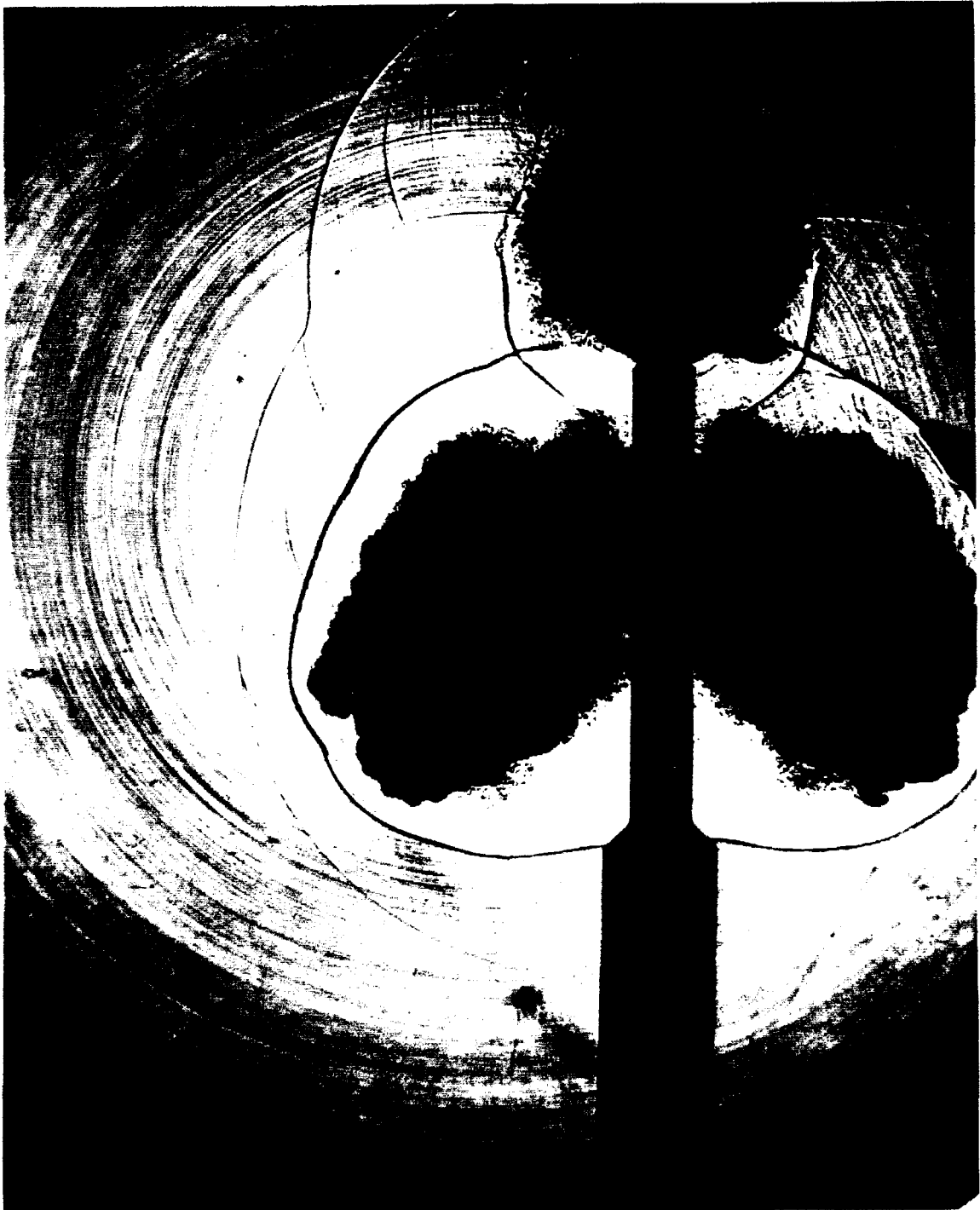


137b. Shadowgraph for round 19540, 120-mm side vent brake, taken with no time delay.

R541 - 30 CAL - (#4) 120MM SIDE VENTS

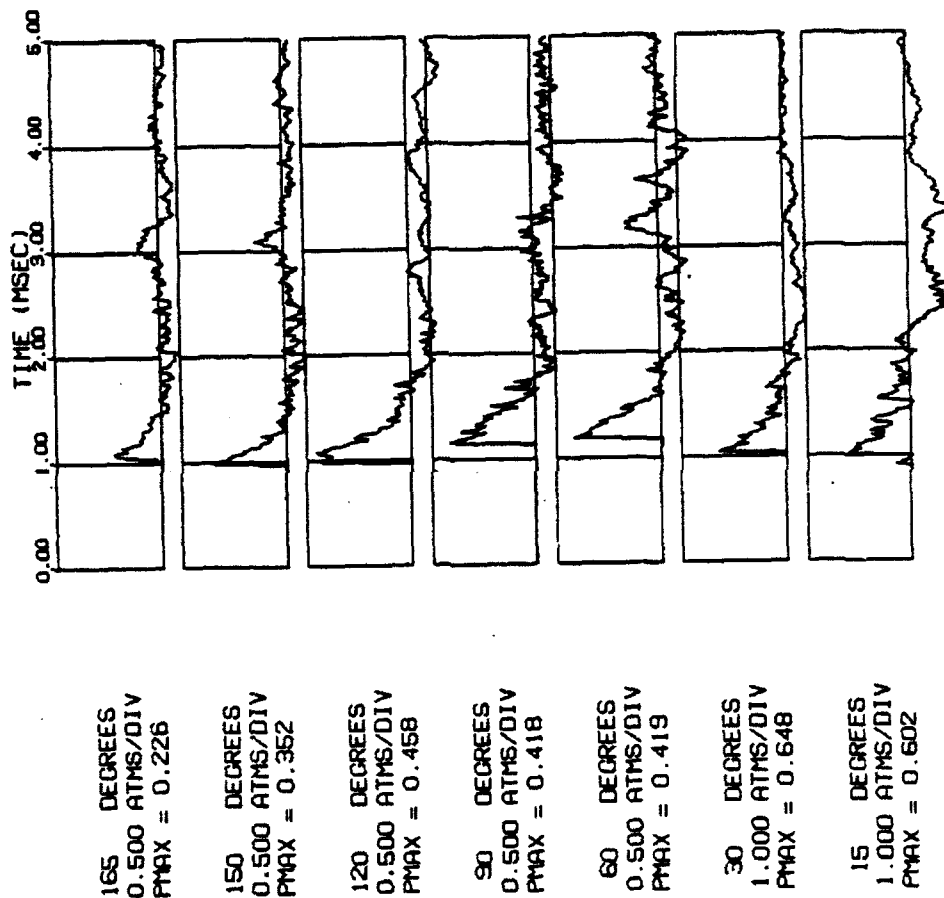


B8a. Pressure histories for round 19541, 120-mm side vent brake at 30 calibers. Data used in report figures.

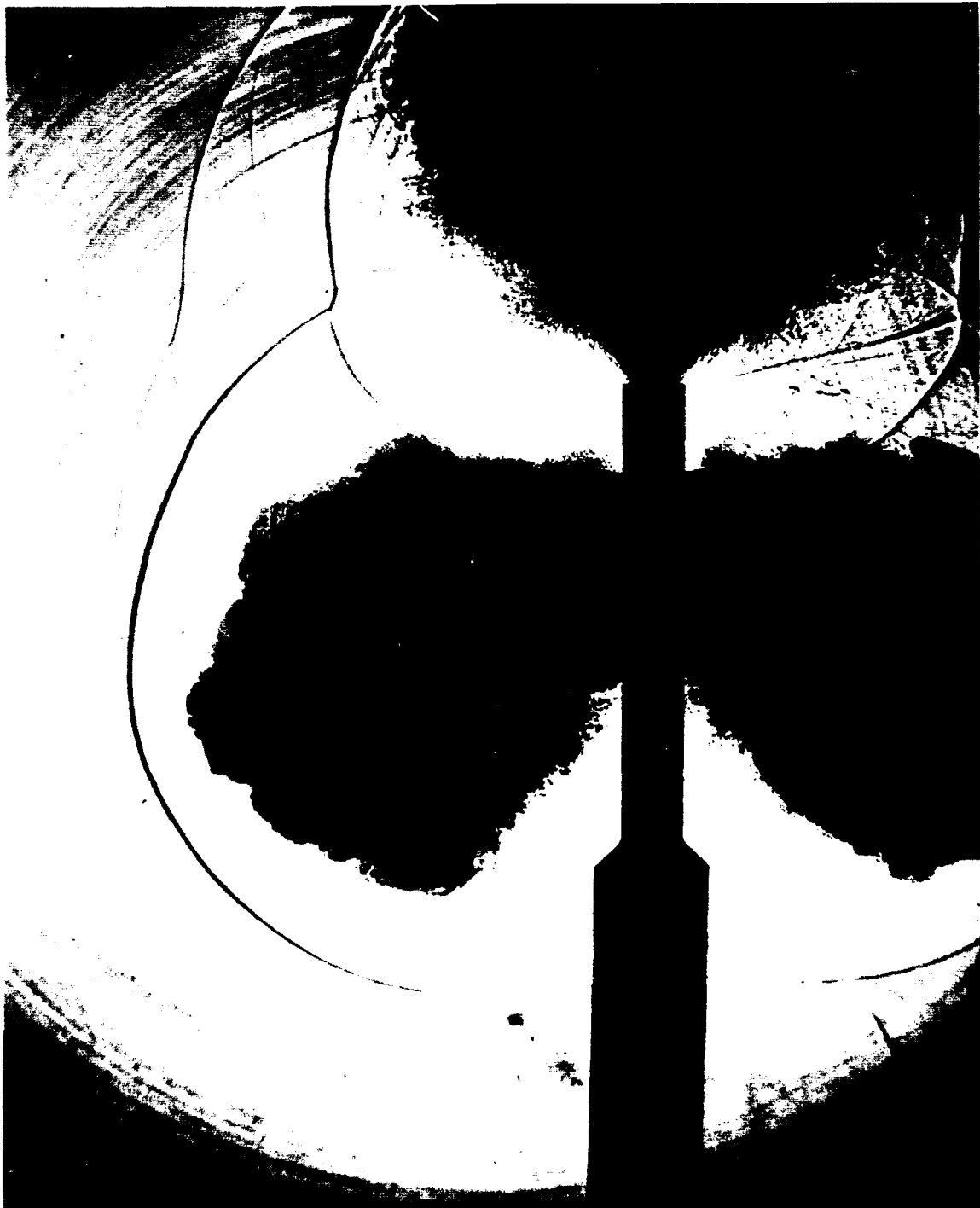


B8b. Shadowgraph for round 19541, 120-mm side vent brake, taken with a 150 microsecond time delay.

R542 - 30 CAL - (#4) 120MM SIDE VENTS

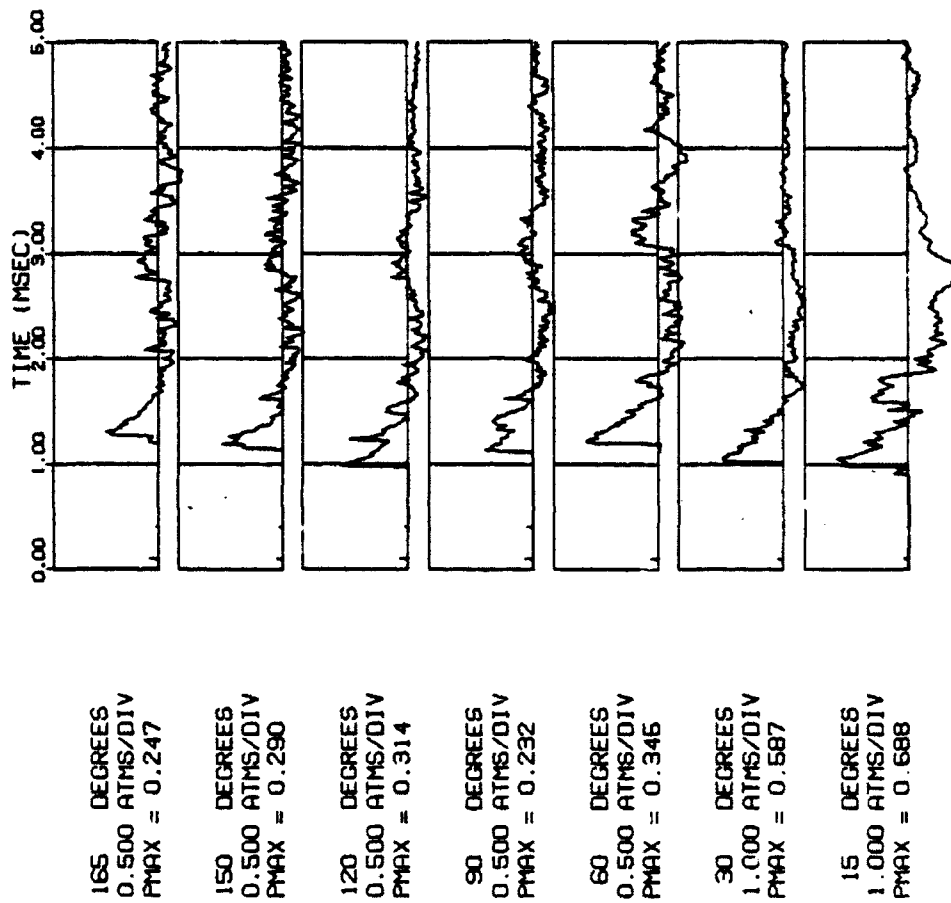


B9a. Pressure histories for round 19542, 120-mm side vent brake at 30 calibers. Data used in report figures.

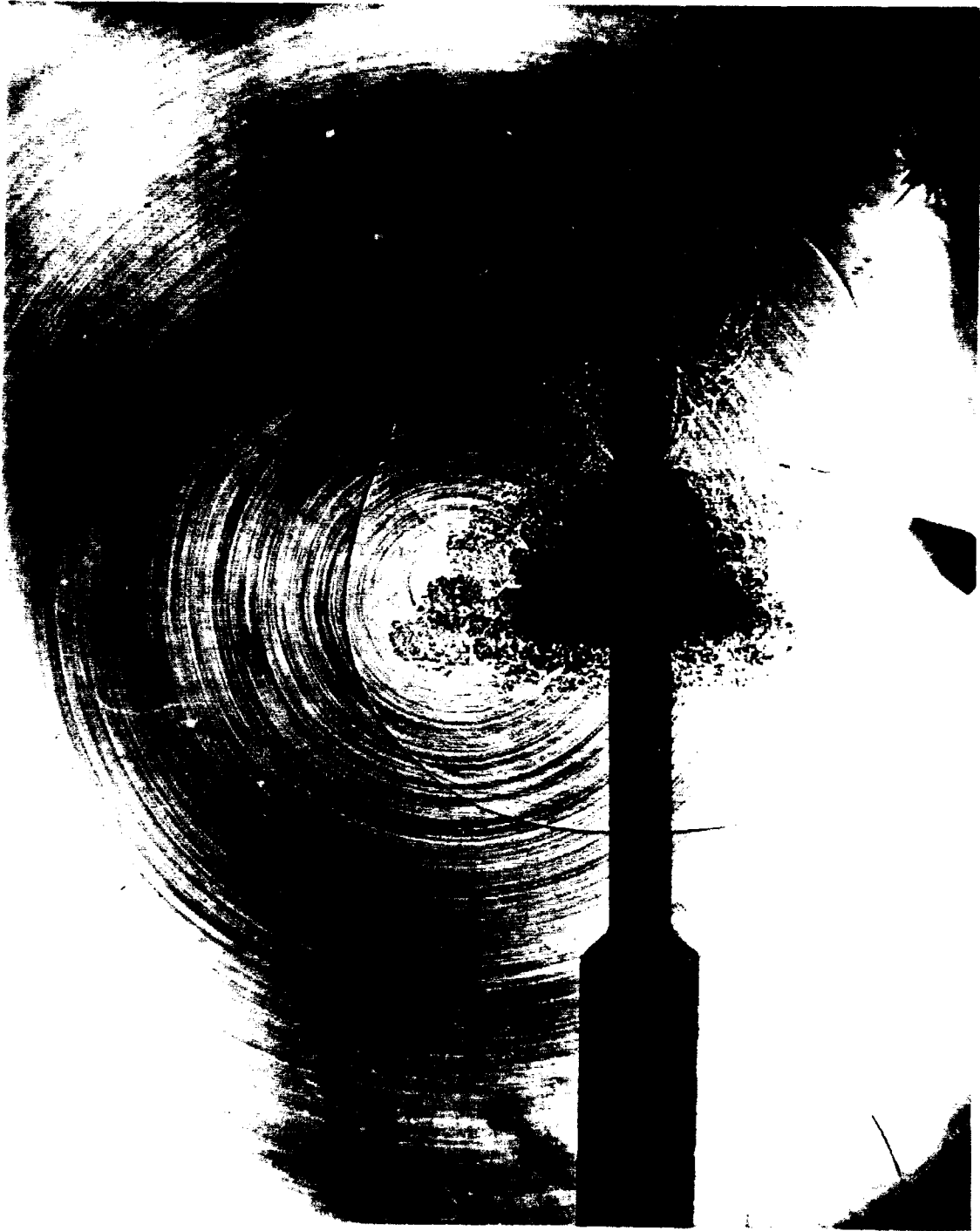


B9b. Shadowgraph for round 19542, 120-mm side vent brake, taken with a 300-microsecond time delay.

RS46 - 30 CAL - (#6) 105MM ELLIPTIC

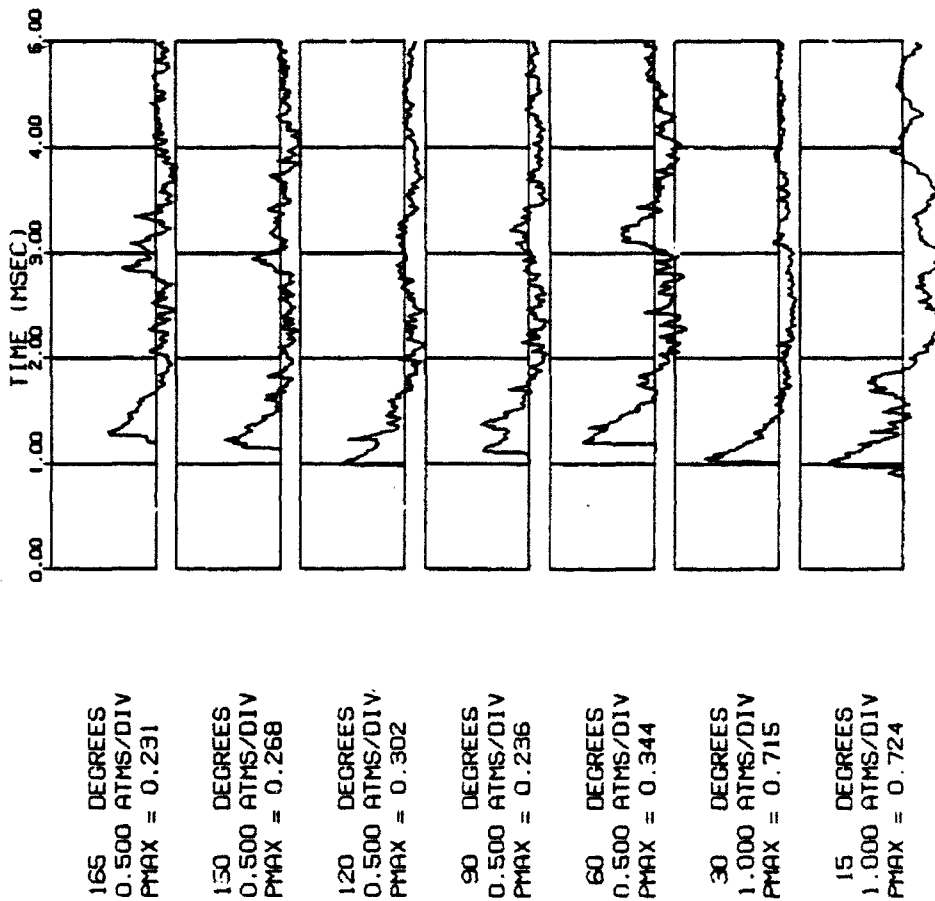


B10a. Pressure histories for round 19546, 105-mm elliptic brake at 30 calibers. Data used in report figures.



B10b. Shadowgraph for round 19546, 105-mm elliptic brake, taken with no time delay.

R547 - 30 CAL - (#6) 105MM ELLIPTIC

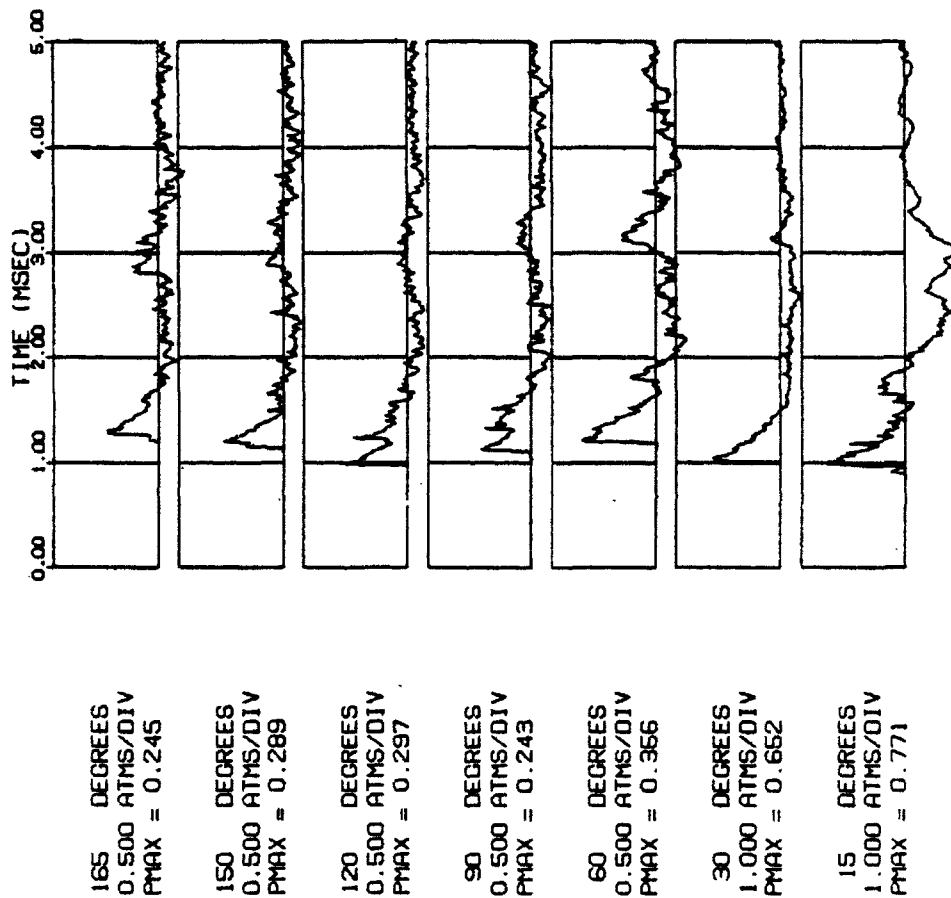


B11a. Pressure histories for round 19547, 105-mm elliptic brake at 30 calibers. Data used in report figures.



B11b. Shadowgraph for round 19547, 105-mm elliptic brake, taken with a 150-microsecond time delay.

R548 - 30 CAL - (#6) 105MM ELLIPTIC

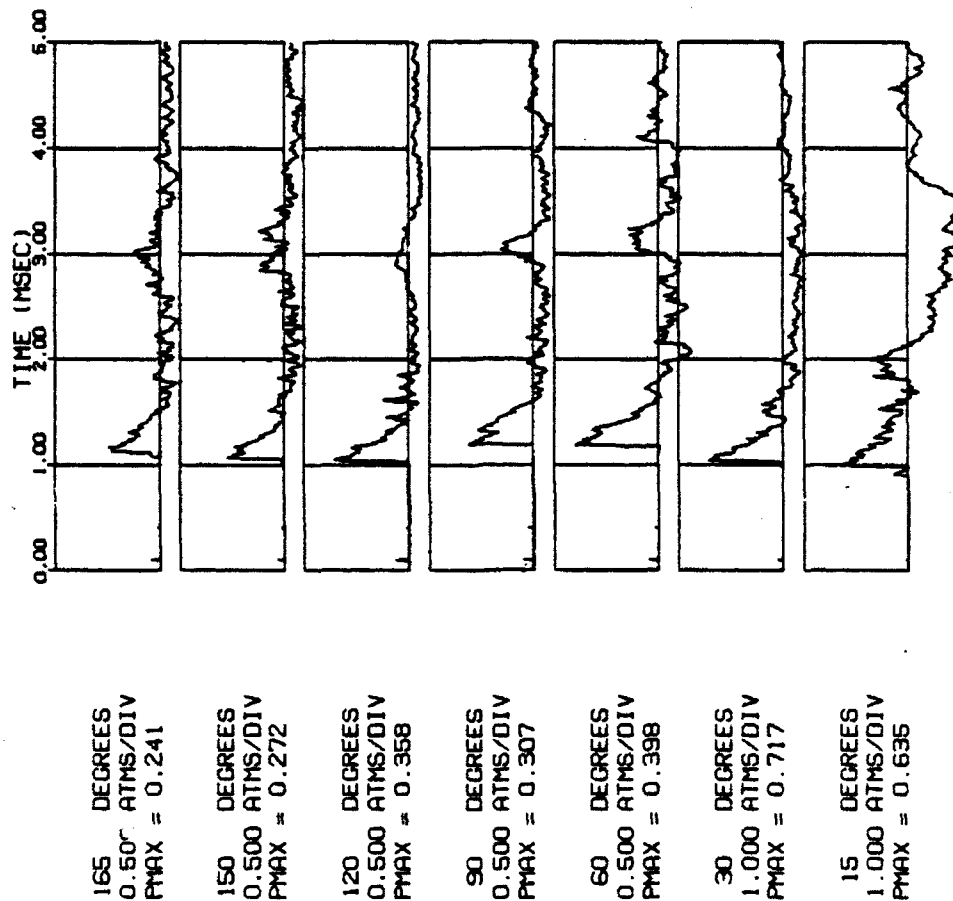


B12a. Pressure histories for round 19548, 105-mm elliptic brake at 30 calibers. Data used in report figures.

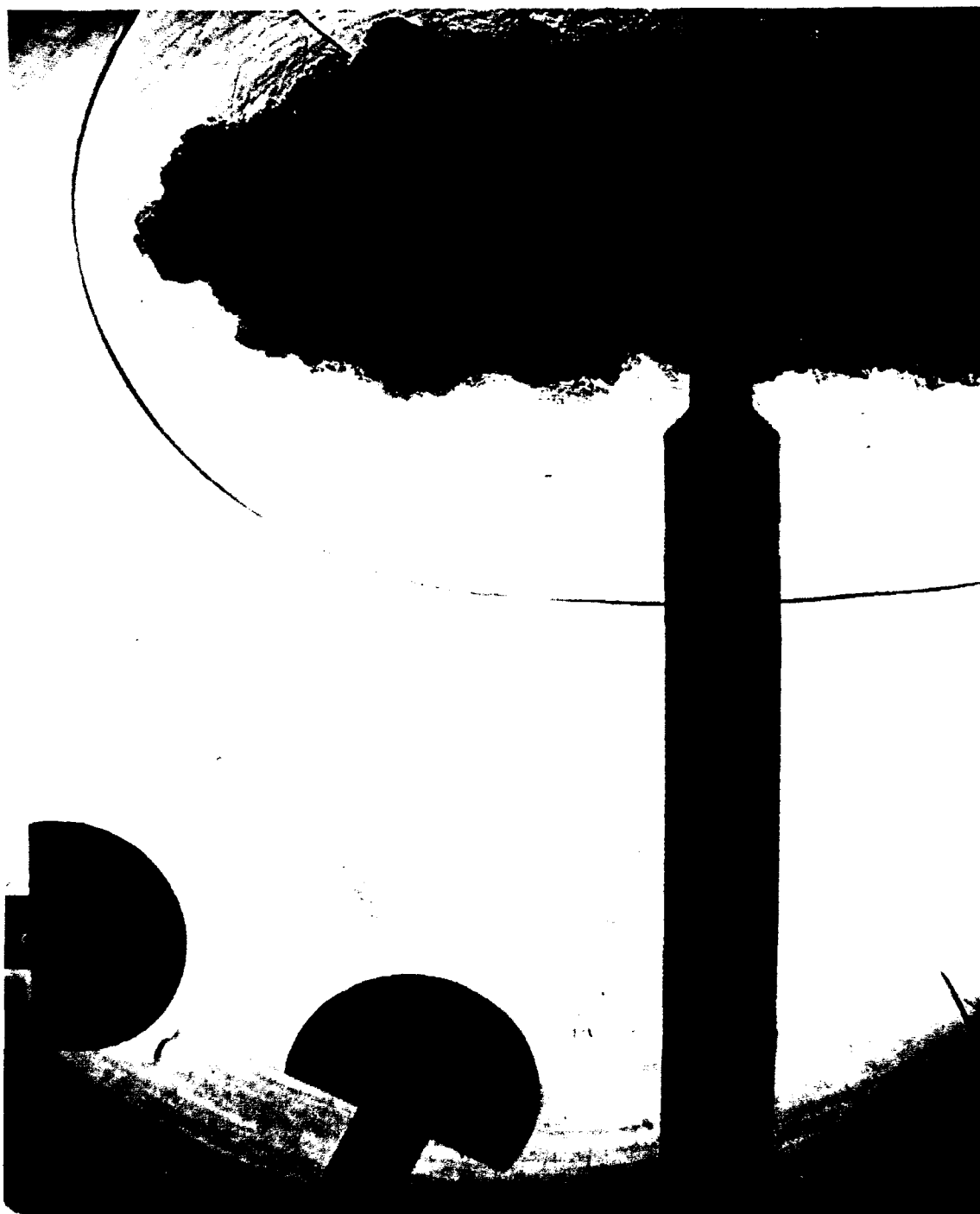


B12b. Shadowgraph for round 19548, 105-mm elliptic brake, taken with a 300-microsecond time delay.

R557 - 30 CAL - (#2) 120MM 4X4

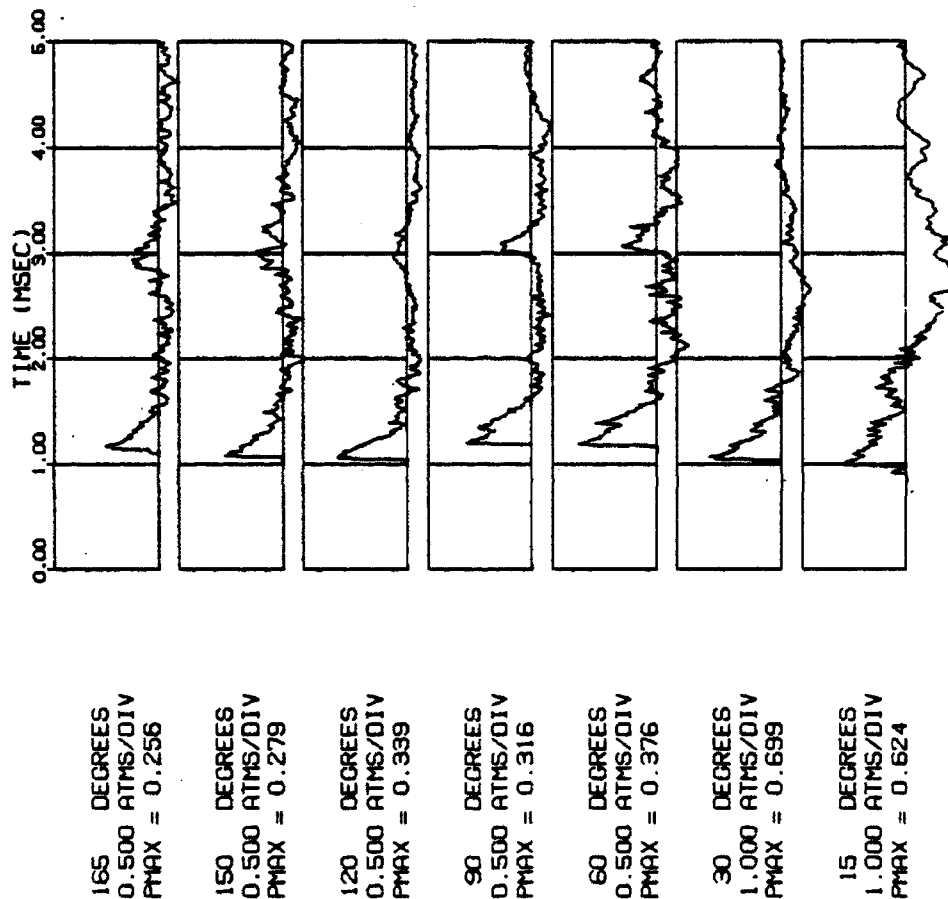


B13a. Pressure histories for round 19557, 120-mm standard brake at 30 calibers. Data used in report figures.



B13b. Shadowgraph for round 19557, 120-mm standard brake, taken with a 450-microsecond time delay.

RS58 - 30 CAL - (#2) 120MM 4X4

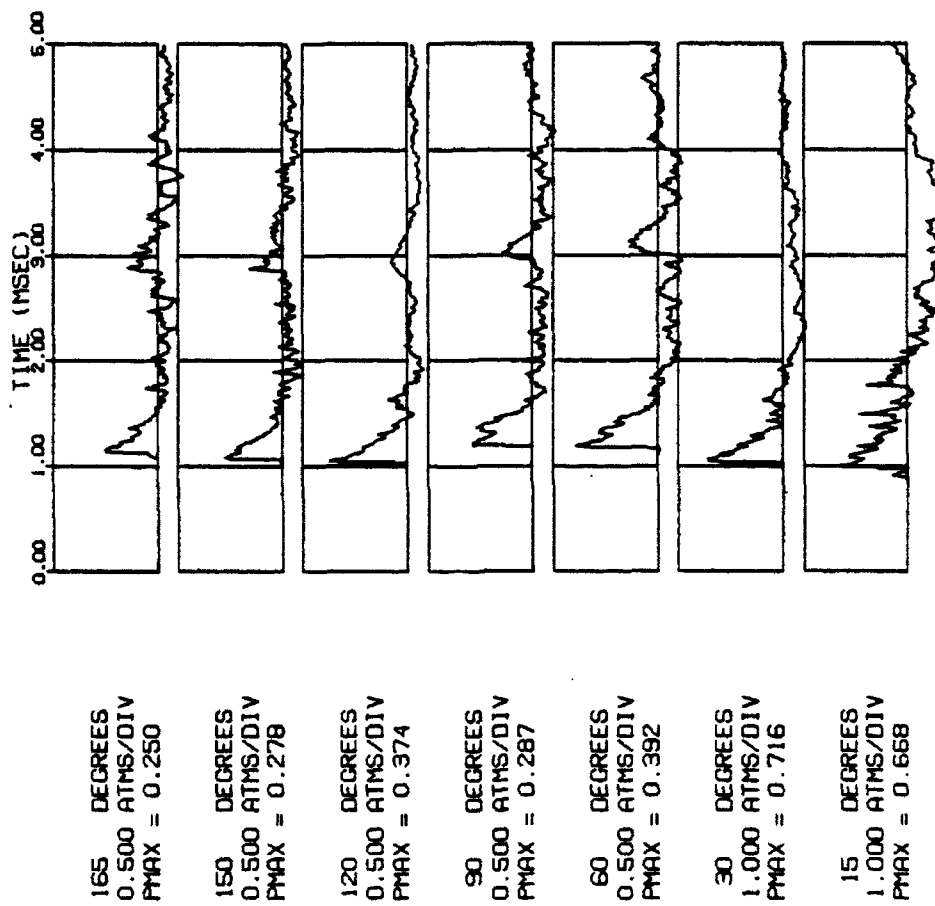


B14a. Pressure histories for round 19558, 120-mm standard brake at 30 calibers. Data used in report figures.



B14b. Shadowgraph for round 19558, 120-mm standard brake, taken with a 600-microsecond time delay.

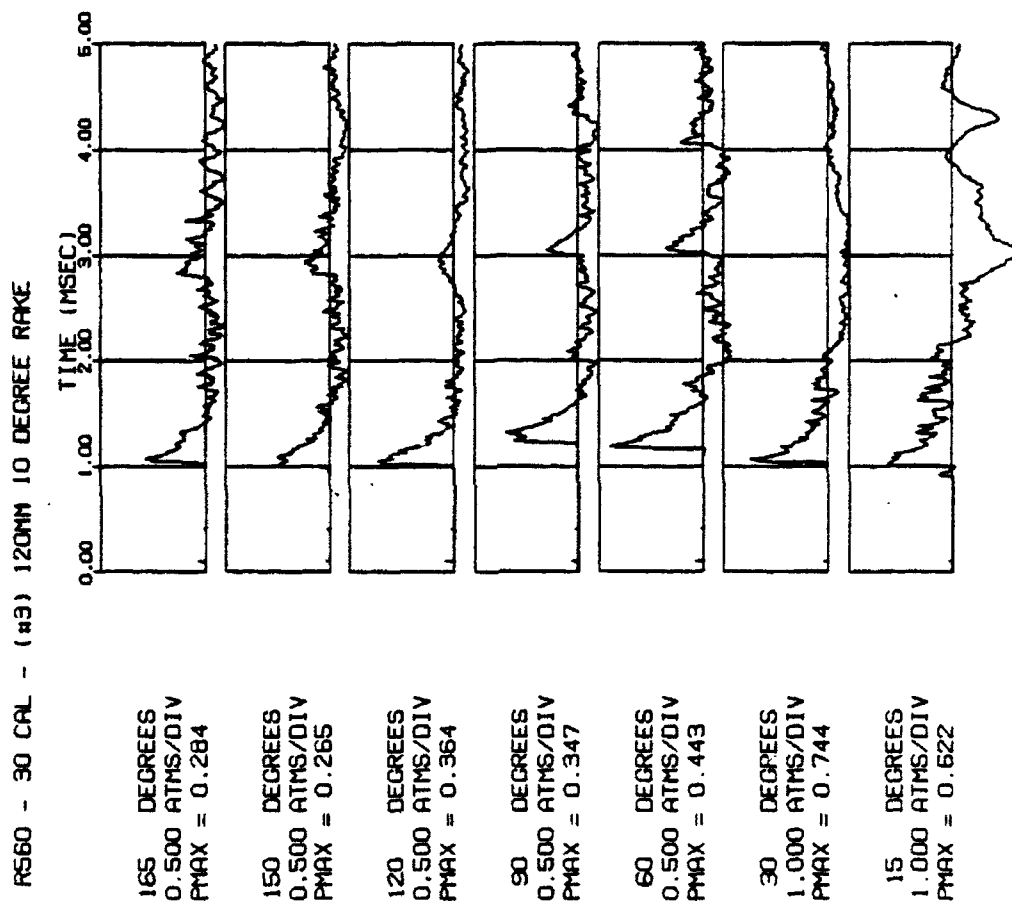
R559 - 30 CAL - (#2) 120MM 4X4



B15a. Pressure histories for round 19559, 120-mm standard brake at 30 calibers. Data used in report figures.



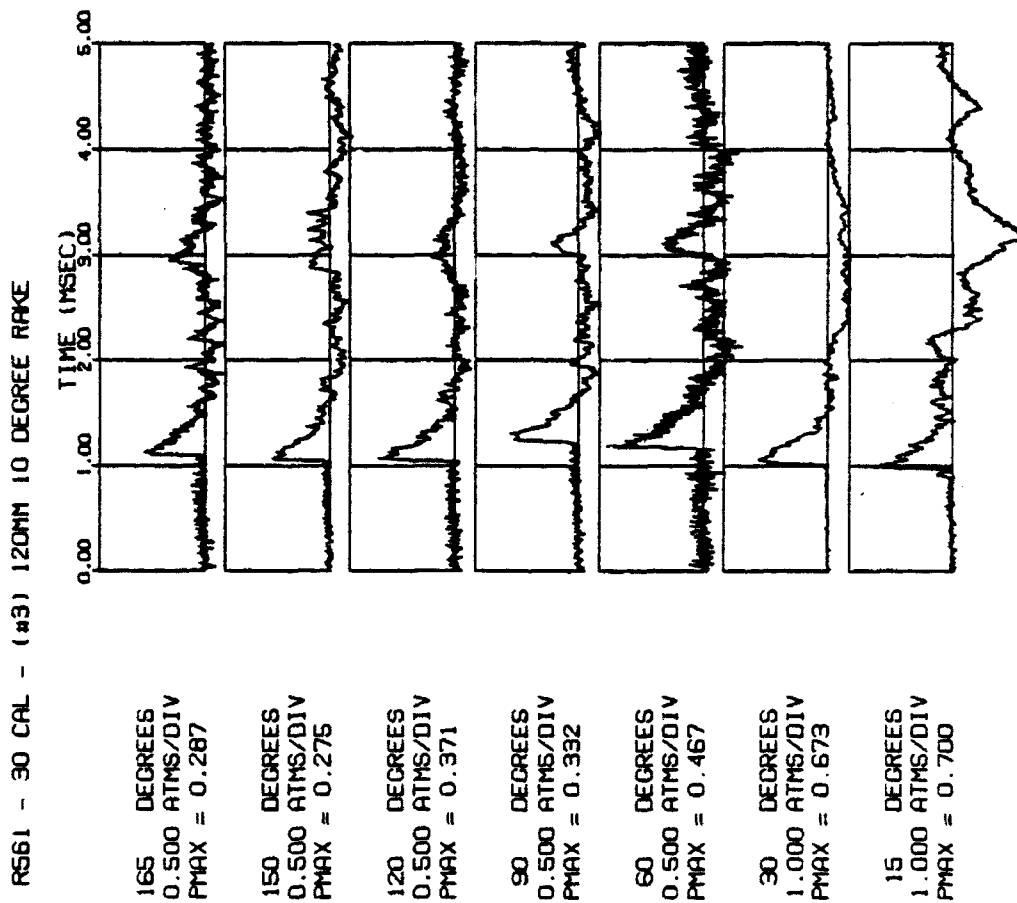
B15b. Shadowgraph for round 19559, 120-mm standard brake, taken with a 750-microsecond time delay.



B16a. Pressure histories for round 19560, 120-mm modified brake at 30 calibers. Data used in report figures.



B16b. Shadowgraph for round 19560, 120-mm modified brake, taken with a 450-microsecond time delay.

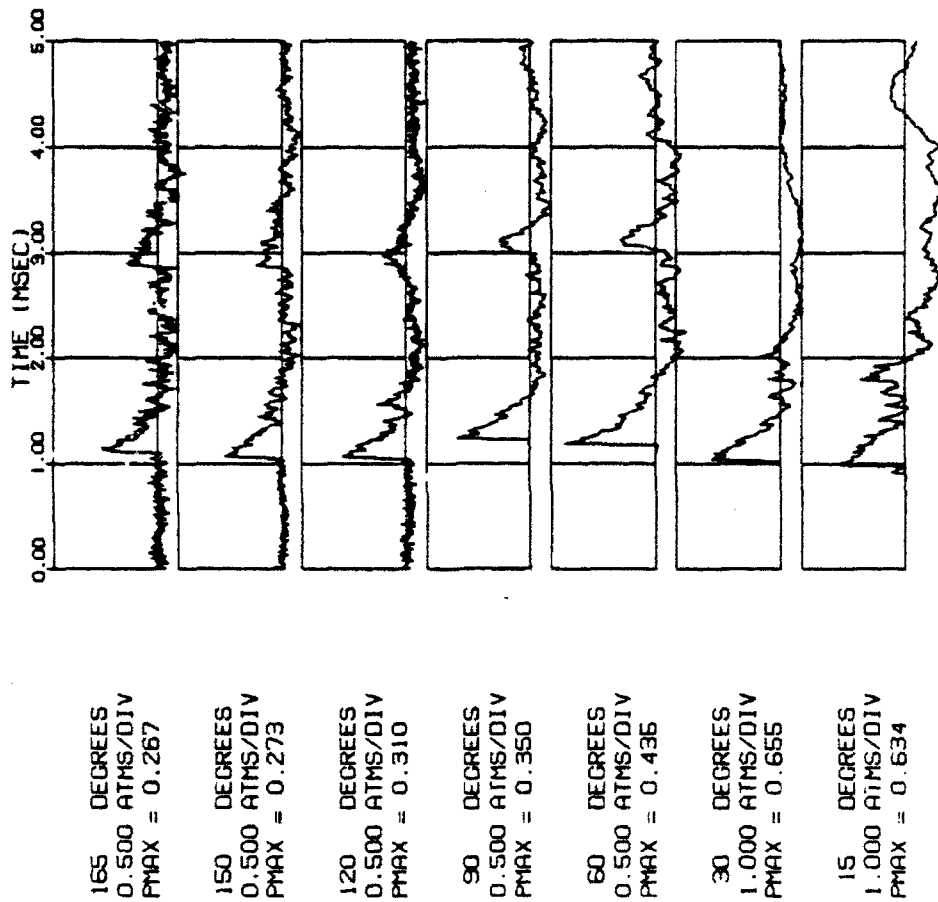


B17a. Pressure histories for round 19561, 120-mm modified brake at 30 calibers. Data used in report figures.



B17b. Shadowgraph for round 19561, 120-mm modified brake, taken with a 600-microsecond time delay.

R562 - 30 CAL - (#3) 120MM 10 DEGREE RAKE

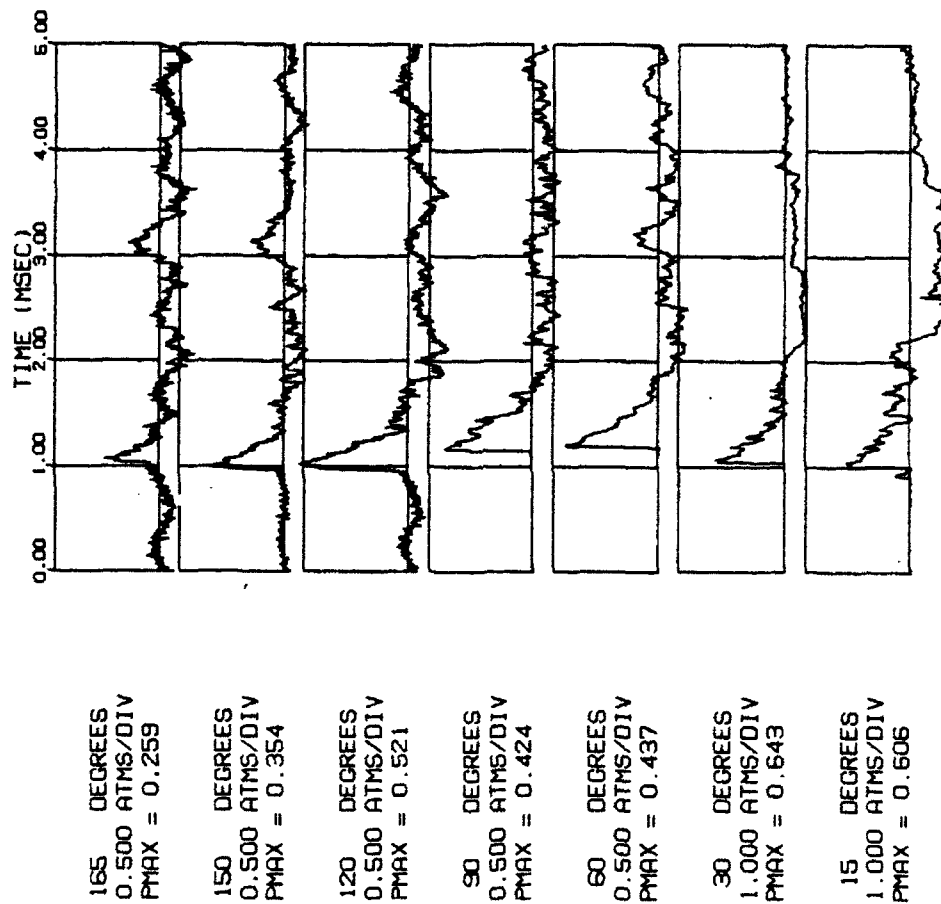


B18a. Pressure histories for round 19562, 120-mm modified brake at 30 calibers. Data used in report figures.



B18b. Shadowgraph for round 19562, 120-mm modified brake, taken with a 750-microsecond time delay.

R563 - 30 CAL - (#4) 120MM SIDE VENTS

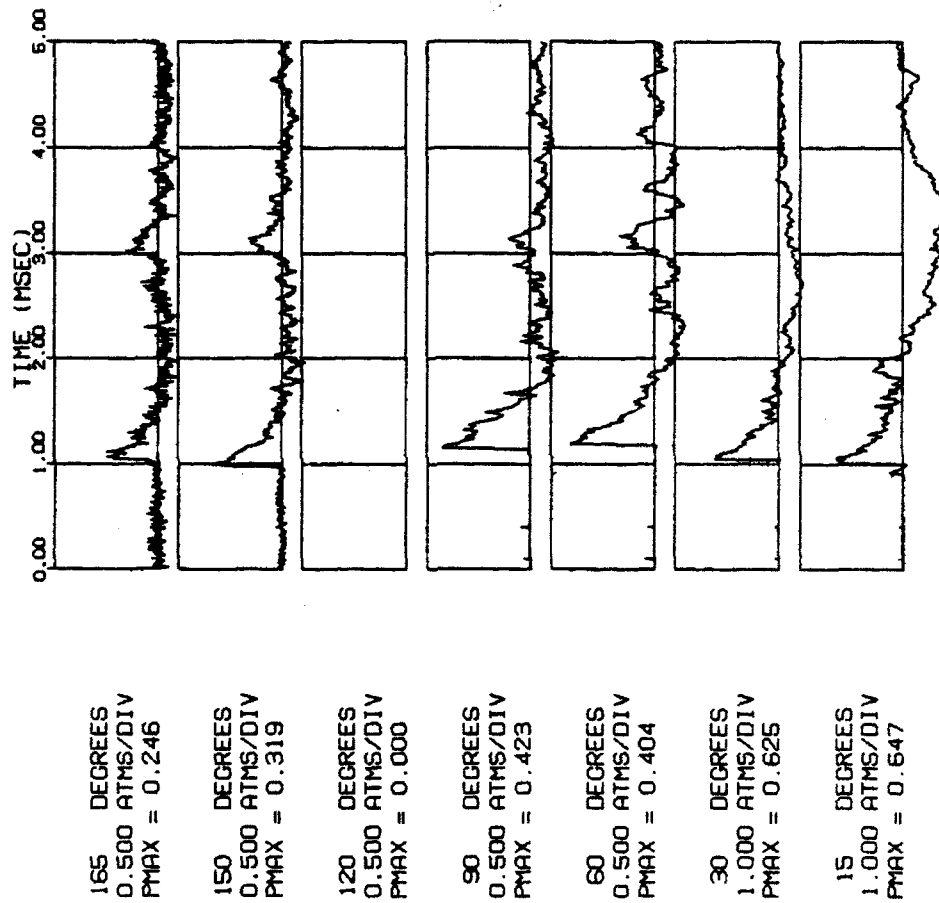


B19a. Pressure histories for round 19563, 120-mm side vent brake at 30 calibers. Data used in report figures.



B19b. Shadowgraph for round 19563, 120-mm side vent brake, taken with a 450-microsecond time delay.

R564 - 30 CAL - (#4) 120MM SIDE VENTS

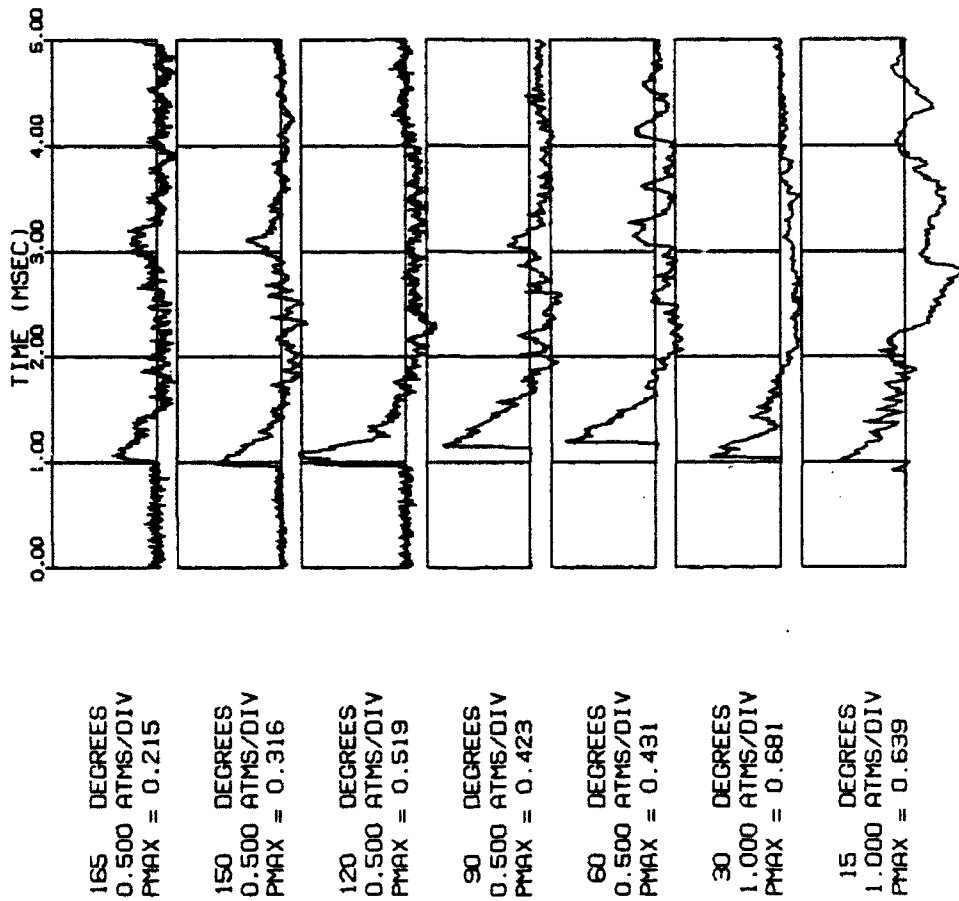


B20a. Pressure histories for round 19564, 120-mm side vent brake at 30 calibers. Data not used in report figures.



B20b. Shadowgraph for round 19564, 120-mm side vent brake, taken with a 600-microsecond time delay.

R565 - 30 CAL - (#4) 120MM SIDE VENTS

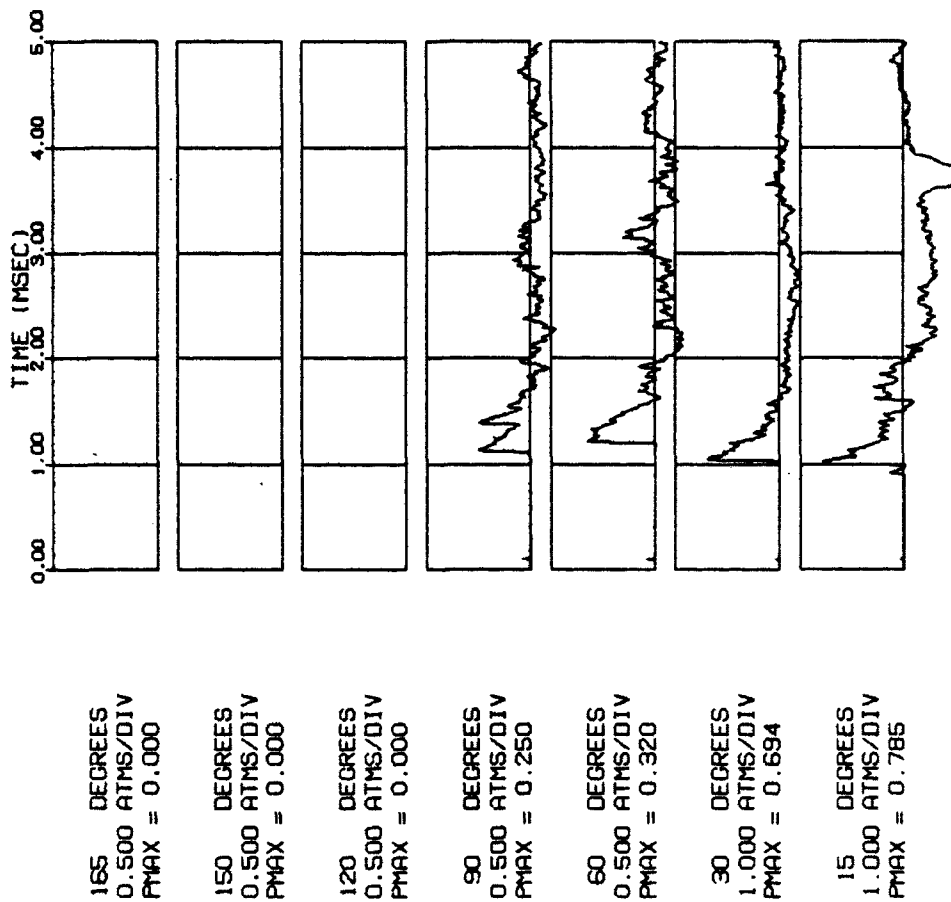


B21a. Pressure histories for round 19565, 120-mm side vent brake at 30 calibers. Data used in report figures.



B21b. Shadowgraph for round 19565, 120-mm side vent brake, taken with a 750-microsecond time delay.

R570 - 30 CAL - (#6) 105MM ELLIPTIC

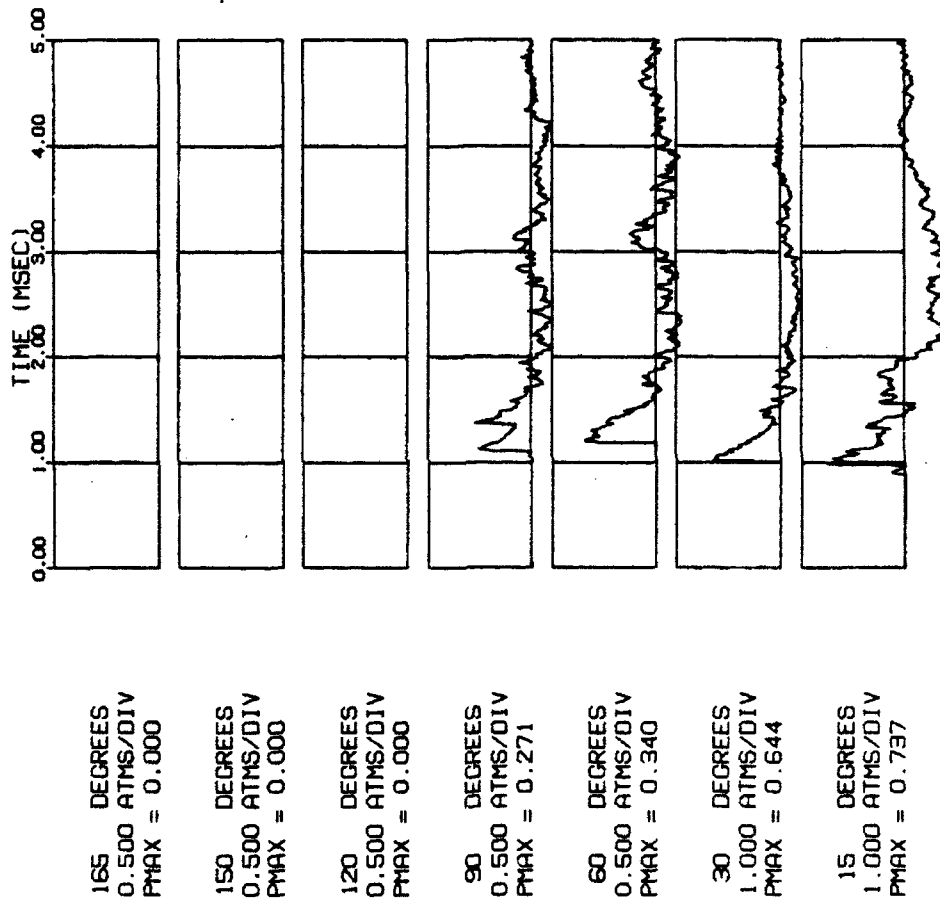


B22a. Pressure histories for round 19570, 105-mm elliptic brake at 30 calibers. Data not used in report figures.

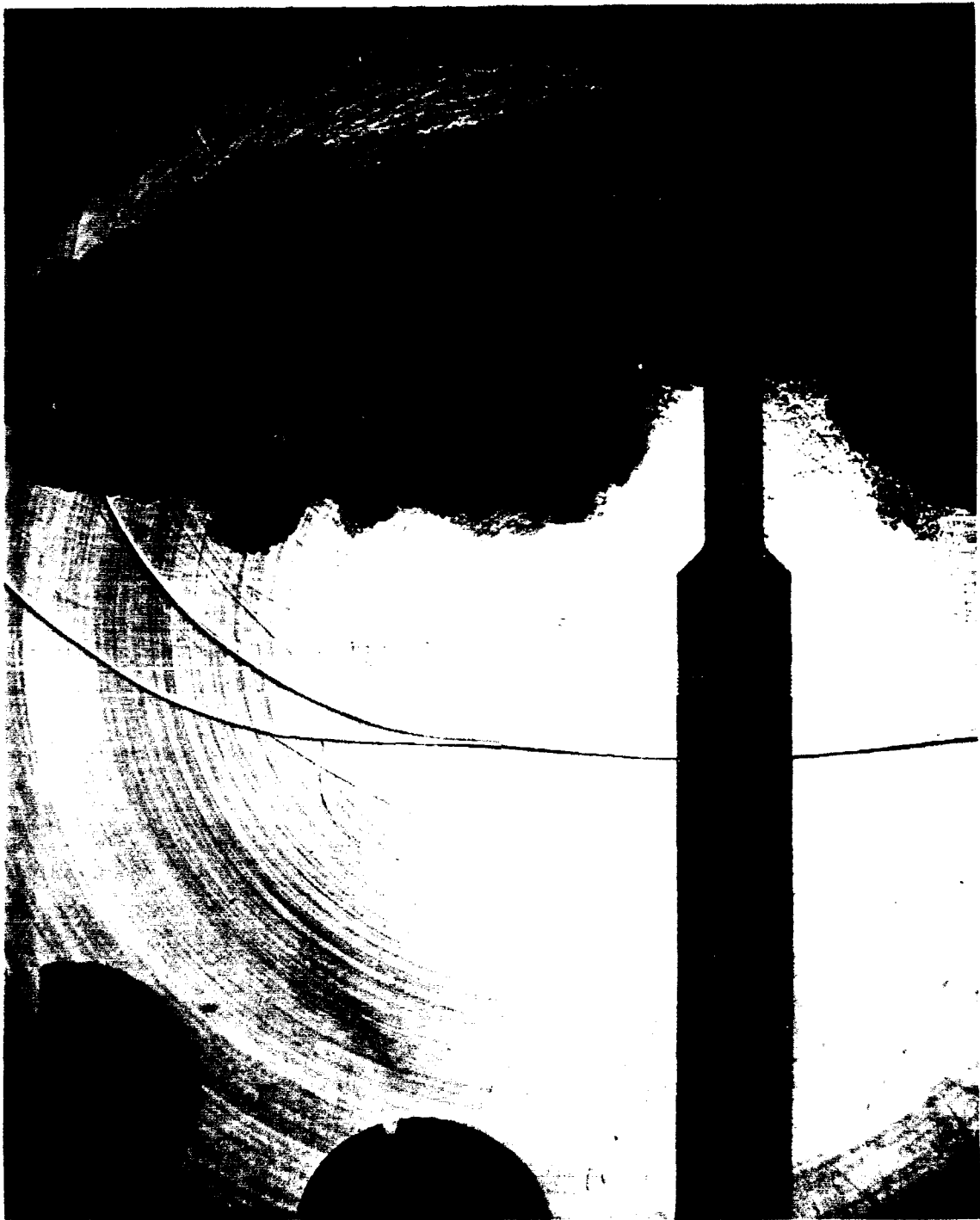


B22b. Shadowgraph for round 19570, 105-mm elliptic brake, taken with a 450-microsecond time delay.

R571 - 30 CAL - (#6) 105MM ELLIPTIC

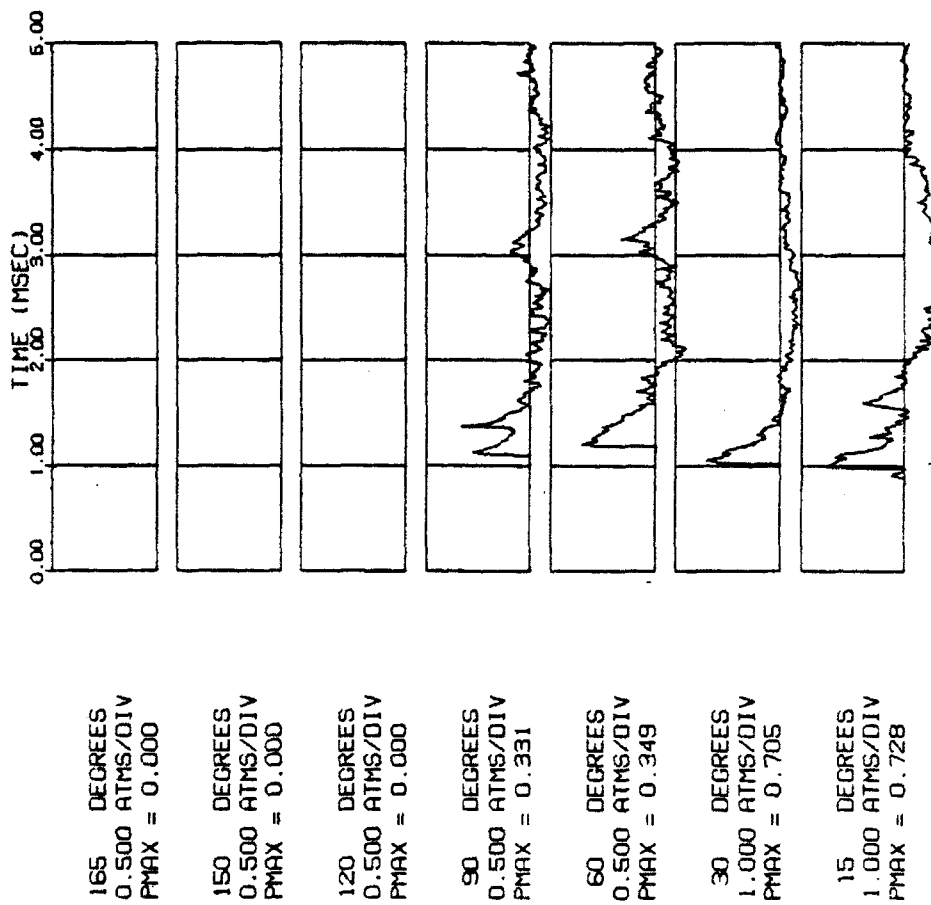


B23a. Pressure histories for round 19571, 105-mm elliptic brake at 30 calibers. Data not used in report figures.



B23b. Shadowgraph for round 19571, 105-mm elliptic brake, taken with a 600-microsecond time delay.

RS72 - 30 CAL - (#6) 105MM ELLIPTIC



B24a. Pressure histories for round 19572, 105-mm elliptic brake at 30 calibers. Data not used in report figures.



B24b. Shadowgraph for round 19572, 105-mm elliptic brake, taken with a 750-microsecond time delay.

APPENDIX C

The data presented in this appendix were obtained in conjunction with a blast reduction study reported elsewhere (ref 21). Fifty-nine rounds were fired in the program, forty-nine of which pertain to this study. The remaining ten rounds refer to a special brake with a split vent pattern. The 'missing round identifiers' in Table C1 below are associated with that brake.

The projectile velocity was measured by a pair of light stations placed downstream which produced an average value 4.6 m from the muzzle. The cannon recoiled freely in the experiment, and the impulse was determined from its mass and terminal velocity.

Table C1. Measured Velocity and Impulse Data

Round	Extension	Velocity (m/sec)	Impulse (nt-sec)
19530	bare muzzle	1060.1	150.1
19531	bare muzzle	1055.5	151.5
19532	bare muzzle	1065.3	153.8
19533	bare muzzle	1051.0	-
19534	120-mm standard	1060.1	128.0
19535	120-mm standard	1058.9	126.5
19536	120-mm standard	1057.4	125.9
19537	120-mm modified	1060.4	125.1
19538	120-mm modified	1060.1	125.1
19539	120-mm modified	1056.4	124.6
19540	120-mm side vent	1058.9	125.5
19541	120-mm side vent	1060.7	125.5
19542	120-mm side vent	1056.4	125.1
19543	105-mm standard	1060.7	122.1
19544	105-mm standard	1060.7	123.0
19545	105-mm standard	1061.0	123.6
19546	105-mm elliptic	1058.0	123.2
19547	105-mm elliptic	1062.8	123.6
19548	105-mm elliptic	1060.4	123.0
19552	bare muzzle	1058.3	149.9
19553	bare muzzle	1058.0	150.5

Table C1. Continued

Round	Extension	Velocity (m/sec)	Impulse (nt-sec)
19554	bare muzzle	1054.9	150.9
19555	bare muzzle	1058.9	151.1
19556	bare muzzle	1056.1	149.9
19557	120-mm standard	1059.8	125.9
19558	120-mm standard	1058.3	125.9
19559	120-mm standard	1062.8	127.1
19560	120-mm modified	1055.2	124.2
19561	120-mm modified	1056.7	123.8
19562	120-mm modified	1049.7	123.0
19563	120-mm side vent	1060.1	127.7
19564	120-mm side vent	1060.4	125.1
19565	120-mm side vent	1058.0	124.7
19566	105-mm standard	1060.4	121.1
19567	105-mm standard	1066.2	119.0
19568	105-mm standard	1056.1	-
19569	105-mm standard	1061.6	120.3
19570	105-mm elliptic	1056.1	122.5
19571	105-mm elliptic	1068.9	124.4
19572	105-mm elliptic	1065.0	120.7
19576	bare muzzle	1055.5	148.8
19577	bare muzzle	1065.0	149.7
19578	bare muzzle	1061.6	149.1
19579	105-mm standard	1057.0	121.1
19580	105-mm standard	1061.0	121.8
19583	bare muzzle	1062.2	149.9
19584	bare muzzle	1065.3	150.1
19585	105-mm standard	1055.5	121.3
19586	105-mm standard	1056.4	120.7

The data in Table C1 were numerically averaged to give the results in Tables C2 and C3 along with the maximum and minimum deviations from the averages. The impulses were not reported for rounds 19533 (bare muzzle) and 19568 (105-mm standard brake), which accounts for the smaller number of rounds in Table C3.

Table C2. Averaged Velocity Data

Extension	Number of Rounds	Velocity (m/sec)	+ Dev (m/sec)	- Dev (m/sec)
bare muzzle	14	1059.1	6.2	-8.2
120-mm standard	6	1059.5	3.3	-2.2
120-mm modified	6	1056.4	4.0	-6.7
120-mm side vent	6	1059.1	1.6	-2.6
105-mm standard	11	1059.7	6.5	-4.2
105-mm elliptic	6	1061.9	7.1	-5.7

Table C3. Averaged Impulse Data

Extension	Number of Rounds	Impulse (nt-sec)	+ Dev (nt-sec)	- Dev (nt-sec)	β
bare muzzle	13	150.4	3.4	-1.6	-
120-mm standard	6	126.5	1.5	-0.7	51.1
120-mm modified	6	124.3	0.8	-1.3	55.9
120-mm side vent	6	125.6	2.0	-0.9	53.0
105-mm standard	10	121.4	2.2	-2.4	62.1
105-mm elliptic	6	122.9	1.5	-2.2	58.9

TECHNICAL REPORT INTERNAL DISTRIBUTION LIST

	NO. OF COPIES
CHIEF, DEVELOPMENT ENGINEERING DIVISION	
ATTN: SMCAR-CCB-DA	1
-DC	1
-DI	1
-DR	1
-DS (SYSTEMS)	1
CHIEF, ENGINEERING SUPPORT DIVISION	
ATTN: SMCAR-CCB-S	1
-SD	1
-SE	1
CHIEF, RESEARCH DIVISION	
ATTN: SMCAR-CCB-R	2
-RA	1
-RE	1
-RM	1
-RP	1
-RT	1
TECHNICAL LIBRARY	5
ATTN: SMCAR-CCB-TL	
TECHNICAL PUBLICATIONS & EDITING SECTION	3
ATTN: SMCAR-CCB-TL	
OPERATIONS DIRECTORATE	1
ATTN: SMCWV-ODP-P	
DIRECTOR, PROCUREMENT DIRECTORATE	1
ATTN: SMCWV-PP	
DIRECTOR, PRODUCT ASSURANCE DIRECTORATE	1
ATTN: SMCWV-QA	

NOTE: PLEASE NOTIFY DIRECTOR, BENET LABORATORIES, ATTN: SMCAR-CCB-TL, OF ANY ADDRESS CHANGES.

TECHNICAL REPORT EXTERNAL DISTRIBUTION LIST

	NO. OF COPIES		NO. OF COPIES
ASST SEC OF THE ARMY RESEARCH AND DEVELOPMENT ATTN: DEPT FOR SCI AND TECH THE PENTAGON WASHINGTON, D.C. 20310-0103	1	COMMANDER ROCK ISLAND ARSENAL ATTN: SMCRI-ENM ROCK ISLAND, IL 61299-5000	1
ADMINISTRATOR DEFENSE TECHNICAL INFO CENTER ATTN: DTIC-FDAC CAMERON STATION ALEXANDRIA, VA 22304-6145	12	MIAC/CINDAS PURDUE UNIVERSITY P.O. BOX 2634 WEST LAFAYETTE, IN 47906	1
COMMANDER US ARMY ARDEC ATTN: SMCAR-AEE	1	COMMANDER US ARMY TANK-AUTMV R&D COMMAND ATTN: AMSTA-ODL (TECH LIB) WARREN, MI 48397-5000	1
SMCAR-AES, BLDG. 321	1	COMMANDER US MILITARY ACADEMY ATTN: DEPARTMENT OF MECHANICS WEST POINT, NY 10996-1792	1
SMCAR-AET-O, BLDG. 351N	1		
SMCAR-CC	1		
SMCAR-CCP-A	1		
SMCAR-FSA	1		
SMCAR-FSM-E	1	US ARMY MISSILE COMMAND REDSTONE SCIENTIFIC INFO CTR ATTN: DOCUMENTS SECT, BLDG. 4484 REDSTONE ARSENAL, AL 35898-5241	2
SMCAR-FSS-D, BLDG. 94	1		
SMCAR-IMI-I (STINFO) BLDG. 59	2		
PICATINNY ARSENAL, NJ 07806-5000			
DIRECTOR US ARMY BALLISTIC RESEARCH LABORATORY ATTN: SLCBR-DD-T, BLDG. 305 ABERDEEN PROVING GROUND, MD 21005-5066	1	COMMANDER US ARMY FGN SCIENCE AND TECH CTR ATTN: DRXST-SD 220 7TH STREET, N.E. CHARLOTTESVILLE, VA 22901	1
DIRECTOR US ARMY MATERIEL SYSTEMS ANALYSIS ACTV ATTN: AMXSY-MP ABERDEEN PROVING GROUND, MD 21005-5071	1	COMMANDER US ARMY LABCOM MATERIALS TECHNOLOGY LAB ATTN: SLCMT-IML (TECH LIB) WATERTOWN, MA 02172-0001	2
COMMANDER HQ, AMCCOM ATTN: AMSMC-IMP-L ROCK ISLAND, IL 61299-6000	1		

NOTE: PLEASE NOTIFY COMMANDER, ARMAMENT RESEARCH, DEVELOPMENT, AND ENGINEERING CENTER, US ARMY AMCCOM, ATTN: BENET LABORATORIES, SMCAR-CCB-TL, WATERVLIET, NY 12189-4050, OF ANY ADDRESS CHANGES.

TECHNICAL REPORT EXTERNAL DISTRIBUTION LIST (CONT'D)

	<u>NO. OF COPIES</u>		<u>NO. OF COPIES</u>
COMMANDER US ARMY LABCOM, ISA ATTN: SLCIS-IM-TL 2800 POWDER MILL ROAD ADELPHI, MD 20783-1145	1	COMMANDER AIR FORCE ARMAMENT LABORATORY ATTN: AFATL/MN EGLIN AFB, FL 32542-5434	1
COMMANDER US ARMY RESEARCH OFFICE ATTN: CHIEF, IPO P.O. BOX 12211 RESEARCH TRIANGLE PARK, NC 27709-2211	1	COMMANDER AIR FORCE ARMAMENT LABORATORY ATTN: AFATL/MNF EGLIN AFB, FL 32542-5434	1
DIRECTOR US NAVAL RESEARCH LAB ATTN: MATERIALS SCI & TECH DIVISION CODE 26-27 (DOC LIB) WASHINGTON, D.C. 20375	1 1	DIRECTOR US ARMY BALLISTIC RESEARCH LABORATORY ATTN: SLCBR-IB-M (DR. BRUCE BURNS) ABERDEEN PROVING GROUND, MD 21005-5066	1

NOTE: PLEASE NOTIFY COMMANDER, ARMAMENT RESEARCH, DEVELOPMENT, AND ENGINEERING CENTER, US ARMY AMCCOM, ATTN: BENET LABORATORIES, SMCAR-CCB-TL, WATERVLIET, NY 12189-4050, OF ANY ADDRESS CHANGES.